Available online at www.sciencedirect.com
SCIENCE DIRECT®
Journal of Computational Physics 205 (2005) 458–485
JOURNAL OF COMPUTATIONAL PHYSICS
www.elsevier.com/locate/jcp

Anti-diffusive flux corrections for high order finite difference WENO schemes

Zhengfu Xu, Chi-Wang Shu *

Division of Applied Mathematics, Brown University, Box F, Providence, RI 02912, USA

Received 11 October 2004; received in revised form 19 November 2004; accepted 19 November 2004
Available online 16 December 2004

Abstract

In this paper, we generalize a technique of anti-diffusive flux corrections, recently introduced by Després and Lagoutière [Journal of Scientific Computing 16 (2001) 479–524] for first-order schemes, to high order finite difference weighted essentially non-oscillatory (WENO) schemes. The objective is to obtain sharp resolution for contact discontinuities, close to the quality of discrete traveling waves which do not smear progressively for longer time, while maintaining high order accuracy in smooth regions and non-oscillatory property for discontinuities. Numerical examples for one and two space dimensional scalar problems and systems demonstrate the good quality of this flux correction. High order accuracy is maintained and contact discontinuities are sharpened significantly compared with the original WENO schemes on the same meshes.
© 2004 Elsevier Inc. All rights reserved.

Keywords: Anti-diffusive flux correction; Sharpening contact discontinuity; High order accuracy; WENO scheme

1. Introduction

In this paper, we are interested in improving the high order finite difference weighted essentially non-oscillatory (WENO) schemes in the resolution of contact discontinuities. We use the fifth-order finite difference WENO scheme in [11] as an example to demonstrate our approach, although the technique can also be used on finite difference WENO schemes of other orders of accuracy [1] and finite volume WENO schemes on rectangular and triangular meshes [10,13,16].

* Corresponding author. Tel.: +1 401 863 2549; fax: +1 401 863 1355.
E-mail addresses: zhengfu@dam.brown.edu (Z. Xu), shu@dam.brown.edu (C.-W. Shu).

0021-9991/$ - see front matter © 2004 Elsevier Inc. All rights reserved.
doi:10.1016/j.jcp.2004.11.014

High order finite difference WENO schemes in [11] were developed based on the successful ENO schemes [9,20,21] and third-order finite volume WENO schemes [13], and have been quite successful in computational fluid dynamics and other applications. They are especially suitable for problems containing both shocks and complicated smooth flow features. For more details, we refer to the lecture notes [18] and the survey paper [19], and the references therein.

However, as a disadvantage of all shock capturing schemes, the high order finite difference WENO schemes in [11] also suffer from a relatively poor resolution of contact discontinuities, comparing with the resolution of shocks. Although in general a higher order method does have sharper contact discontinuity resolution than lower order methods, and the resolution can often be improved by using a better Riemann solver or flux splitting, it is still in general not easy to stop the progressively more severe smearing for longer simulation time, and at the same time to maintain non-oscillatory property and high order accuracy of the scheme. This is particularly challenging in two or more spatial dimensions.

There have been a lot of efforts in the literature to overcome this problem. Harten [7] proposed the artificial compression method, which modifies the numerical flux so that the numerical characteristics, instead of being in parallel or diverging from the contact discontinuity, converge slightly towards the contact discontinuity to keep its sharpness. Of course, this compression must be done carefully so that stability and accuracy are not lost, and smooth parts of the solution are not evolved to small staircases. This idea was later generalized by Yang [28] to higher order finite volume ENO schemes, via a slope modification. The approach of Yang [28] maintains higher order accuracy of the original ENO scheme while significantly sharpens contact discontinuities. Yang's approach was also applied to finite difference ENO schemes [21] and WENO schemes [1,11] with equally good results. However, two-dimensional results using this approach are less satisfactory. Another successful strategy is Harten's subcell resolution idea [8], which uses two pieces of different polynomial reconstructions in the discontinuity cell, instead of the usual single polynomial reconstruction in a cell, in order not to smear the discontinuity. This strategy works well for one-dimensional problems [8,21]. However, it seems to be difficult to generalize this idea to multi-dimensional problems, except for some special situations, e.g. [22].

More recently, Després and Lagoutière [3] proposed a new approach called limited downwind scheme, much akin to a class of flux limiters by Sweby [24], to prevent the smearing of contact discontinuities while keeping non-linear stability. Their scheme is identical with the ultrabee scheme developed by Roe [15] in the case of linear advection. By introducing an anti-diffusive flux, it gives remarkably sharp profile of contact discontinuities in both one-dimensional scalar and system cases. More importantly, they observe numerically and prove theoretically that their scheme adopts a class of *moving* traveling wave solutions exactly. This has an important implication that the smearing of contact discontinuities will not be progressively more severe for larger time, but will be stabilized for all time. A later paper by Bouchut [2] further modifies this scheme to satisfy entropy conditions and also gives a simple explicit formula for this limited downwind anti-diffusive flux.

Even though the schemes in [2,3] are quite attractive, they are only first-order accurate and are not suitable for computing solutions containing both discontinuities and complex smooth flow features. Our objective in this paper is to develop an anti-diffusive flux correction technique, based on the approach of [2,3], to high order finite difference WENO schemes in [1,11]. We would like the resulting scheme to maintain high order accuracy in smooth regions, non-oscillatory behavior near discontinuities, and sharp contact discontinuity resolution similar to the first-order schemes in [2,3] which does not progressively become worse for larger time.

The first-order schemes developed in [2,3] use simple Euler forward time discretization. For our high order finite difference schemes, we will need to use high order total variation diminishing (TVD) Runge–Kutta time discretizations [20]. It is more difficult to maintain sharp contact discontinuity resolution with multi-stage high order Runge–Kutta methods. We will need to introduce adjustments in each stage of the Runge–Kutta methods in order to overcome this difficulty.

We would like to remark that recently, Toro and Titarev initialized an approach to use second-order two-point TVD fluxes, which are less dissipative than first-order monotone fluxes, as building blocks for higher order Godunov type schemes [26,25]. Their numerical results show an improvement, sometimes dramatic, on numerical resolutions when such fluxes are used. Our current work has the same philosophy of using less dissipative low order fluxes as building blocks for higher order extensions. We use, however, first-order anti-diffusive fluxes of more than two points, hence the traditional Godunov procedure does not apply and a careful extension to higher order schemes must be made to maintain accuracy, stability and sharpening of contact discontinuities simultaneously.

This paper is organized as follows. In Section 2, we briefly review the first-order limited downwind flux of [3], using the form in [2]. In Section 3, we present the modified fifth-order WENO scheme with third-order Runge–Kutta time discretization for one-dimensional problems. In Section 4, we present our schemes in two dimensions. In Section 5, we show extensive numerical results to demonstrate the behavior of our approach. Concluding remarks are given in Section 6.

2. First-order limited downwind anti-diffusive scheme for one-dimensional conservation laws

In this section, we briefly review the first-order limited downwind flux of [3], using the form in [2]. We consider a one-dimensional scalar conservation law

$$u_t + f(u)_x = 0 \tag{2.1}$$

with $t > 0$, $x \in R$ and $f'(u) \geqslant 0$. The procedure for the case with $f'(u) \leqslant 0$ is completely symmetric.

An explicit conservative fully discrete finite difference/finite volume scheme (there is no need to distinguish between them for first- and second-order schemes) has the form

$$u_i^{n+1} - u_i^n + \lambda_i\left(\hat{f}^n_{i+\frac{1}{2}} - \hat{f}^n_{i-\frac{1}{2}}\right) = 0, \tag{2.2}$$

where u_i^n is the approximation either to the point value $u(x_i, t^n)$ (finite difference) or to the cell average $\frac{1}{\Delta x_i}\int_{x_{i-\frac{1}{2}}}^{x_{i+\frac{1}{2}}} u(x,t^n)\,dx$ (finite volume), $\lambda_i = \Delta t/\Delta x_i$ is the local CFL number, and $\hat{f}^n_{i+\frac{1}{2}}$ is the numerical flux. We will often drop the superscript n which refers to the time step and denote by u_i, $\hat{f}_{i+\frac{1}{2}}$ instead of u_i^n, $\hat{f}^n_{i+\frac{1}{2}}$, respectively, when there is no ambiguity. A basic result about the numerical flux stated in [2] is

Proposition 2.1. *Assume that the usual CFL condition $\lambda_i f'(u) \leqslant 1$ holds, and the numerical flux satisfies*

$$\hat{f}_{i+\frac{1}{2}} \in \left[\hat{f}^{\mathrm{diss}}_{i+\frac{1}{2}}, \hat{f}^{\mathrm{l}}_{i+\frac{1}{2}}\right] \bigcap \left[\hat{f}^{\mathrm{diss}}_{i+\frac{1}{2}}, \hat{f}^{\mathrm{r}}_{i+\frac{1}{2}}\right], \tag{2.3}$$

where

$$\hat{f}^{\mathrm{diss}}_{i+\frac{1}{2}} = f(u_i), \quad \hat{f}^{\mathrm{l}}_{i+\frac{1}{2}} = \frac{u_i - u_{i-1}}{\lambda_i} + f(u_{i-1}), \quad \hat{f}^{\mathrm{r}}_{i+\frac{1}{2}} = f(u_{i+1}), \tag{2.4}$$

then the scheme (2.2) satisfies the maximum principle

$$\min_k u_k^n \leqslant u_i^{n+1} \leqslant \max_k u_k^n,$$

and is total variation diminishing (TVD)

$$\mathrm{TV}(u^{n+1}) \leqslant \mathrm{TV}(u^n), \quad \text{where} \quad \mathrm{TV}(u) \equiv \sum_i |u_{i+1} - u_i|.$$

Here and below, we use the notation $[a,b]$ to denote the closed interval $[\min(a,b), \max(a,b)]$. The dissipative flux $\hat{f}^{\mathrm{diss}}$ is the classical upwind flux, and fluxes $\hat{f}^{\mathrm{l}}$ and $\hat{f}^{\mathrm{r}}$ are the extremal leftwind and rightwind fluxes, in the sense that $u_i - \lambda_i(\hat{f}^{\mathrm{l}}_{i+\frac{1}{2}} - \hat{f}^{\mathrm{diss}}_{i-\frac{1}{2}}) = u_{i-1}$, $u_i - \lambda_i(\hat{f}^{\mathrm{diss}}_{i+\frac{1}{2}} - \hat{f}^{\mathrm{r}}_{i-\frac{1}{2}}) = u_i$.

Next we give the definition of the limited downwind flux in [3].

Definition 2.2. The limited downwind flux $\hat{f}^{\mathrm{a}}_{i+\frac{1}{2}}$ is defined by

$$\left[\hat{f}^{\mathrm{diss}}_{i+\frac{1}{2}}, \hat{f}^{\mathrm{l}}_{i+\frac{1}{2}}\right] \bigcap \left[\hat{f}^{\mathrm{diss}}_{i+\frac{1}{2}}, \hat{f}^{\mathrm{r}}_{i+\frac{1}{2}}\right] = \left[\hat{f}^{\mathrm{diss}}_{i+\frac{1}{2}}, \hat{f}^{\mathrm{a}}_{i+\frac{1}{2}}\right]. \tag{2.5}$$

It can be easily verified that an equivalent form of this limited downwind flux is

$$\hat{f}^{\mathrm{a}}_{i+\frac{1}{2}} = \hat{f}^{\mathrm{diss}}_{i+\frac{1}{2}} + \mathrm{minmod}\left(\hat{f}^{\mathrm{l}}_{i+\frac{1}{2}} - \hat{f}^{\mathrm{diss}}_{i+\frac{1}{2}}, \hat{f}^{\mathrm{r}}_{i+\frac{1}{2}} - \hat{f}^{\mathrm{diss}}_{i+\frac{1}{2}}\right), \tag{2.6}$$

by an explicit calculation of different cases. It can also be rewritten as, using (2.4)

$$\hat{f}^{\mathrm{a}}_{i+\frac{1}{2}} = f(u_i) + \mathrm{minmod}\left(\frac{u_i - u_{i-1}}{\lambda_i} + f(u_{i-1}) - f(u_i), f(u_{i+1}) - f(u_i)\right). \tag{2.7}$$

Here, as usual, the minmod function is defined by

$$\mathrm{minmod}(a,b) = \begin{cases} 0 & ab \leqslant 0, \\ a & ab > 0, \ \ |a| \leqslant |b|, \\ b & ab > 0, \ \ |a| > |b|. \end{cases}$$

The equivalent form (2.7) is the one we are going to use for the construction of our high order extension, since it allows for this extension to maintain both high order accuracy and stability.

The scheme with the limited downwind flux $\hat{f}^{\mathrm{a}}$ satisfies the following attractive property, proved in [3].

Proposition 2.3. *The scheme (2.2) with the limited downwind flux $\hat{f}^{\mathrm{a}}$ defined in (2.7), applied to a linear advection equation*

$$u_t + a u_x = 0, \tag{2.8}$$

where $a > 0$ is a constant, maintains a class of traveling wave solutions: for any initial condition which is piecewise constant with each piece containing at least three grid points, under the CFL condition $a\lambda = a\frac{\Delta t}{\Delta x} \leqslant 1$, the numerical solution will not have more than one transition point between two constant pieces.

This property guarantees that, for such initial conditions (or for other initial conditions which can evolve into such shapes), the numerical solution will maintain its shape for all time and will not progressively smear discontinuities more severely for longer time.

We will also consider a relaxed anti-diffusive flux in the following form:

$$\hat{f}^{\mathrm{a}}_{i+\frac{1}{2}} = f(u_i) + \varphi_i \mathrm{minmod}\left(\frac{u_i - u_{i-1}}{\lambda_i} + f(u_{i-1}) - f(u_i), f(u_{i+1}) - f(u_i)\right), \tag{2.9}$$

where φ_i is a discontinuity indicator between 0 and 1. Ideally, to apply the anti-diffusive modification to the upwind flux only near a discontinuity, φ_i should be close to 0 in smooth regions and close to 1 near a discontinuity. Our choice of φ_i will be described in Section 3.3. When $0 \leqslant \varphi_i \leqslant 1$, by Proposition 2.1, we can see that the scheme (2.2) with the flux (2.9) still satisfies the maximum principle and is a TVD scheme.

Another observation in designing high order extensions of this scheme is related to the time discretization. First-order explicit Euler method can no longer be used, but higher order multi-stage Runge–Kutta methods have additional difficulties in coupling with the sharpening procedure. This issue will be addressed in next section.

3. Modified high order WENO finite difference scheme in one dimension

In this section, we extend the first-order sharpening procedure to higher order WENO finite difference schemes in one dimension. We will first discuss the modification of the first-order anti-diffusive flux when coupled with high order multi-stage Runge–Kutta time discretization.

3.1. Second- and third-order TVD Runge–Kutta time discretization

The second-order TVD Runge–Kutta time discretization [20] is given by

$$\begin{aligned} u^{(1)} &= u^n + \Delta t L(u^n), \\ u^{n+1} &= \frac{1}{2}u^n + \frac{1}{2}u^{(1)} + \frac{1}{2}\Delta t L(u^{(1)}), \end{aligned} \tag{3.1}$$

where L is the spatial discretization of $-f(u)_x$. This can be rewritten as

$$\begin{aligned} u^{(1)} &= u^n + \Delta t L(u^n), \\ u^{n+1} &= u^n + \frac{1}{2}\Delta t L(u^n) + \frac{1}{2}\Delta t L(u^{(1)})a. \end{aligned} \tag{3.2}$$

In order to maintain the moving traveling wave solutions for piecewise constant functions containing contact discontinuities as in the Euler forward case, we would need to modify the scheme (3.2) by

$$\begin{aligned} u^{(1)} &= u^n + \Delta t L(u^n), \\ u^{n+1} &= u^n + \frac{1}{2}\Delta t L'(u^n) + \frac{1}{2}\Delta t L(u^{(1)}), \end{aligned} \tag{3.3}$$

where the operator L is defined as

$$L(u)_i = -\lambda_i\left(\hat{f}^{\mathrm{a}}_{i+\frac{1}{2}} - \hat{f}^{\mathrm{a}}_{i-\frac{1}{2}}\right), \tag{3.4}$$

with the anti-diffusive flux $\hat{f}^{\mathrm{a}}$ given by (2.7), and the operator L' is defined as

$$L'(u)_i = -\lambda_i\left(\bar{f}^{\mathrm{a}}_{i+\frac{1}{2}} - \bar{f}^{\mathrm{a}}_{i-\frac{1}{2}}\right), \tag{3.5}$$

with the modified anti-diffusive flux $\bar{f}^{\mathrm{a}}$ given by

$$\bar{f}^{\mathrm{a}}_{i+\frac{1}{2}} = \begin{cases} f(u_i) + \operatorname{minmod}\left(\frac{2(u_i-u_{i-1})}{\lambda_i} + f(u_{i-1}) - f(u_i), f(u_{i+1}) - f(u_i)\right), & bc > 0, \ \ |b| < |c|, \\ \hat{f}^{\mathrm{a}}, & \text{otherwise}, \end{cases} \tag{3.6}$$

where $b = (u_i - u_{i-1})/\lambda_i + f(u_{i-1}) - f(u)$, $c = f(u_{i+1}) - f(u_i)$.

The scheme (3.3) with L and L' defined by (3.4) and (3.5) is clearly first-order accurate in space and second-order accurate in time. The purpose of the extra factor 2 in the first argument of the minmod function in the definition of $\bar{f}^{\mathrm{a}}$ is to compensate for the coefficient $\frac{1}{2}$ in front of L', so that the final scheme can still maintain exactly traveling wave solutions of a piecewise constant function. To be more precise, numerical experiments show that, for a piecewise constant function with each piece containing at least four grid points, the numerical solution does not have more than two transition points between two constant pieces for the CFL condition $a\lambda = a\frac{\Delta t}{\Delta x} \leqslant \frac{1}{2}$. A larger CFL number (up to 0.58 by our numerical experiments) can be used to obtain sharp contact discontinuity resolution, although occasionally with more than two transition points between two constant pieces. For example, when $a\lambda = 0.4$ and the initial condition is a step function

$$u_j^0 = \begin{cases} 1, & j \leqslant 0, \\ 0, & \text{otherwise.} \end{cases} \tag{3.7}$$

The sequence of the numerical solution for the first few time steps are: after one-time step

$$u_j^1 = \begin{cases} 1, & j \leqslant 0, \\ 0.4, & j = 1, \\ 0, & \text{otherwise,} \end{cases}$$

after two-time steps

$$u_j^2 = \begin{cases} 1, & j \leqslant 0, \\ 0.7, & j = 1, \\ 0.1, & j = 2, \\ 0, & \text{otherwise,} \end{cases}$$

after three-time steps

$$u^3 = \begin{cases} 1, & j \leqslant 0, \\ 0.88, & j = 1, \\ 0.32, & j = 2, \\ 0, & \text{otherwise,} \end{cases}$$

after four-time steps

$$u^4 = \begin{cases} 1, & j \leqslant 1, \\ 0.6, & j = 2, \\ 0, & \text{otherwise,} \end{cases}$$

after five-time steps

$$u_j^5 = \begin{cases} 1, & j \leqslant 1, \\ 0.8, & j = 2, \\ 0.2, & j = 3, \\ 0, & \text{otherwise,} \end{cases}$$

after six-time steps

$$u_j^6 = \begin{cases} 1, & j \leqslant 1, \\ 0.96, & j = 2, \\ 0.44, & j = 3, \\ 0, & \text{otherwise,} \end{cases}$$

after seven-time steps

$$u_j^7 = \begin{cases} 1, & j \leqslant 2, \\ 0.7, & j = 3, \\ 0.1, & j = 4, \\ 0, & \text{otherwise.} \end{cases}$$

Clearly $u_j^7 = u_{j-2}^2$, hence the numerical solution repeats itself after five-time steps with a shift. If $a\lambda$ is not a rational number, the numerical solution will not exactly repeat after finitely many time steps, but the number of transition points will not be larger than two.

The third-order TVD Runge–Kutta method in [20] has the following form:

$$\begin{aligned} u^{(1)} &= u^n + \Delta t L(u^n), \\ u^{(2)} &= \frac{3}{4}u^n + \frac{1}{4}u^{(1)} + \frac{1}{4}\Delta t L(u^{(1)}), \\ u^{n+1} &= \frac{1}{3}u^n + \frac{2}{3}u^{(2)} + \frac{2}{3}\Delta t L(u^{(2)}), \end{aligned} \tag{3.8}$$

which can be rewritten as

$$\begin{aligned} u^{(1)} &= u^n + \Delta t L(u^n), \\ u^{(2)} &= u^n + \frac{1}{4}\Delta t L(u^n) + \frac{1}{4}\Delta t L(u^{(1)}), \\ u^{n+1} &= u^n + \frac{1}{6}\Delta t L(u^n) + \frac{1}{6}\Delta t L(u^{(1)}) + \frac{2}{3}\Delta t L(u^{(2)}). \end{aligned} \tag{3.9}$$

Again, in order to maintain the moving traveling wave solutions for piecewise constant functions containing contact discontinuities as in the Euler forward case, we would need to modify the scheme (3.9) by

$$\begin{aligned} u^{(1)} &= u^n + \Delta t L(u^n), \\ u^{(2)} &= u^n + \frac{1}{4}\Delta t L'(u^n) + \frac{1}{4}\Delta t L(u^{(1)}), \\ u^{n+1} &= u^n + \frac{1}{6}\Delta t L''(u^n) + \frac{1}{6}\Delta t L(u^{(1)}) + \frac{2}{3}\Delta t L(u^{(2)}), \end{aligned} \tag{3.10}$$

where the operator L is defined by (3.4) with the anti-diffusive flux $\hat{f}^{\mathrm{a}}$ given by (2.7), the operator L' is defined by (3.5) with the modified anti-diffusive flux $\bar{f}^{\mathrm{a}}$ given by

$$\bar{f}^{\mathrm{a}}_{i+\frac{1}{2}} = \begin{cases} f(u_i) + \operatorname{minmod}\left(\frac{4(u_i - u_{i-1})}{\lambda_i} + f(u_{i-1}) - f(u_i), f(u_{i+1}) - f(u_i)\right), & bc > 0, \ \ |b| < |c|, \\ \hat{f}^{\mathrm{a}}, & \text{otherwise}, \end{cases}$$

and the operator L'' is defined by

$$L''(u)_i = -\lambda_i\left(\tilde{f}^{\mathrm{a}}_{i+\frac{1}{2}} - \tilde{f}^{\mathrm{a}}_{i-\frac{1}{2}}\right) \tag{3.11}$$

with the modified anti-diffusive flux $\tilde{f}^{\mathrm{a}}$ given by

$$\tilde{f}^{\mathrm{a}}_{i+\frac{1}{2}} = \begin{cases} f(u_i) + \operatorname{minmod}\left(\frac{6(u_i - u_{i-1})}{\lambda_i} + f(u_{i-1}) - f(u_i), f(u_{i+1}) - f(u_i)\right), & bc > 0, \ \ |b| < |c| \\ \hat{f}^{\mathrm{a}}, & \text{otherwise}. \end{cases}$$

Here again $b = (u_i - u_{i-1})/\lambda_i + f(u_{i-1}) - f(u)$, $c = f(u_{i+1}) - f(u_i)$.

The scheme (3.10) with L, L' and L'' defined by (3.4), (3.5) and (3.11) is clearly first-order accurate in space and third-order accurate in time. The purpose of the extra factor 4 in the first argument of the minmod function in the definition of $\bar{f}^{\mathrm{a}}$ and the extra factor 6 in the first argument of the minmod function in the definition of $\tilde{f}^{\mathrm{a}}$ is again to compensate for the coefficients 1/4 and 1/6 in front of L' and L'', respectively, so that the final scheme can still maintain exactly traveling wave solutions of a piecewise constant function. To be more precise, numerical experiments show that, for a piecewise constant function with each piece containing at least four grid points, the numerical solution does not have more than two transition points

between two constant pieces for the CFL number $a\lambda = a\frac{\Delta t}{\Delta x}$ up to about 0.45. For example, when $a\lambda = 0.3$ and the initial condition the step function (3.7), we can verify that $u_j^{12} = u_{j-3}^2$, namely the numerical solution repeats itself after 10-time steps with a shift. Again, if $a\lambda$ is not a rational number, the numerical solution will not exactly repeat after finitely many time steps, but the number of transition points will not be larger than two.

3.2. Anti-diffusive flux with high order WENO finite difference reconstruction

We now discuss the modification of the high order WENO finite difference fluxes to obtain the anti-diffusive effect. We refer to [11] for the details of the construction of the finite difference WENO flux and will not repeat them here. The high order WENO finite difference fluxes will be denoted by $\hat{f}^-_{i+\frac{1}{2}}$ and $\hat{f}^+_{i+\frac{1}{2}}$, for the two upwind biased fluxes based on stencils with one more point to the left and to the right, respectively. For WENO-Roe schemes [11], the numerical flux is chosen as $\hat{f}^-_{i+\frac{1}{2}}$ when $f'(u) > 0$ and as $\hat{f}^+_{i+\frac{1}{2}}$ when $f'(u) \leqslant 0$.

The modification of the WENO fluxes for the anti-diffusive effects starts with the choice of an anti-diffusive flux similar to (2.7)

$$\hat{f}^{\mathrm{a}}_{i+\frac{1}{2}} = \hat{f}^-_{i+\frac{1}{2}} + \mathrm{minmod}\left(\frac{u_i - u_{i-1}}{\lambda_i} + \hat{f}^-_{i-\frac{1}{2}} - \hat{f}^-_{i+\frac{1}{2}}, \hat{f}^+_{i+\frac{1}{2}} - \hat{f}^-_{i+\frac{1}{2}}\right). \tag{3.12}$$

Or, when the discontinuity indicator φ_i is taken into consideration, the anti-diffusive flux takes the form

$$\hat{f}^{\mathrm{a}}_{i+\frac{1}{2}} = \hat{f}^-_{i+\frac{1}{2}} + \varphi_i \mathrm{minmod}\left(\frac{u_i - u_{i-1}}{\lambda_i} + \hat{f}^-_{i-\frac{1}{2}} - \hat{f}^-_{i+\frac{1}{2}}, \hat{f}^+_{i+\frac{1}{2}} - \hat{f}^-_{i+\frac{1}{2}}\right). \tag{3.13}$$

Notice that the only change we have made is to replace the first-order fluxes in (2.7) and (2.9) by the higher order WENO fluxes.

We remark that the correction to the original WENO flux is no larger in magnitude than that of $\hat{f}^+_{i+\frac{1}{2}} - \hat{f}^-_{i+\frac{1}{2}}$, which is on the level of truncation errors for the WENO schemes because both $\hat{f}^+_{i+\frac{1}{2}}$ and $\hat{f}^-_{i+\frac{1}{2}}$ are high order approximations to the same physical flux at the same location. This guarantees that the modification does not destroy the original high order accuracy of the WENO schemes.

When the WENO scheme is discretized by a Runge–Kutta time discretization, for example if the third-order TVD Runge–Kutta method (3.8) is used, we will again use the modified version (3.10), with the numerical fluxes corresponding to L, L' and L'' defined by (3.13), by

$$\bar{f}^{\mathrm{a}}_{i+\frac{1}{2}} = \begin{cases} \hat{f}^-_{i+\frac{1}{2}} + \mathrm{minmod}\left(\frac{4(u_i - u_{i-1})}{\lambda_i} + \hat{f}^-_{i-\frac{1}{2}} - \hat{f}^-_{i+\frac{1}{2}}, \hat{f}^+_{i+\frac{1}{2}} - \hat{f}^-_{i+\frac{1}{2}}\right), & bc > 0, \ \ |b| < |c|, \\ \hat{f}^{\mathrm{a}}, & \text{otherwise}, \end{cases}$$

and by

$$\tilde{f}^{\mathrm{a}}_{i+\frac{1}{2}} = \begin{cases} \hat{f}^-_{i+\frac{1}{2}} + \mathrm{minmod}\left(\frac{6(u_i - u_{i-1})}{\lambda_i} + \hat{f}^-_{i-\frac{1}{2}} - \hat{f}^-_{i+\frac{1}{2}}, \hat{f}^+_{i+\frac{1}{2}} - \hat{f}^-_{i+\frac{1}{2}}\right), & bc > 0, \ \ |b| < |c|, \\ \hat{f}^{\mathrm{a}}, & \text{otherwise}, \end{cases}$$

respectively. Here $b = \frac{u_i - u_{i-1}}{\lambda_i} + \hat{f}^-_{i-\frac{1}{2}} - \hat{f}^-_{i+\frac{1}{2}}$ and $c = \hat{f}^+_{i+\frac{1}{2}} - \hat{f}^-_{i+\frac{1}{2}}$.

3.3. The discontinuity indicator

As mentioned before, we would like to design the discontinuity indicator φ_i such that it is close to 0 in smooth regions and close to 1 near a discontinuity. After extensive numerical experiments, we have settled on the following choice of the discontinuity indicator φ_i for our numerical tests

$$\varphi_i = \frac{\beta_i}{\beta_i + \gamma_i}, \tag{3.14}$$

where

$$\alpha_i = |u_{i-1} - u_i|^2 + \varepsilon, \quad \beta_i = \left(\frac{\alpha_i}{\alpha_{i-1}} + \frac{\alpha_{i+1}}{\alpha_{i+2}}\right)^2, \quad \gamma_i = \frac{|u_{\max} - u_{\min}|^2}{\alpha_i}, \tag{3.15}$$

where ε is a small positive number taken as 10^{-6} in our numerical experiments, and $u_{\max}$ and $u_{\min}$ are the maximum and minimum values of u_j for all grid points. Clearly, $0 \leqslant \varphi_i \leqslant 1$, and $\varphi_i = O(\Delta x^2)$ in smooth regions. Near a strong discontinuity, $\gamma_i \ll \beta_i$, φ_i is close to 1.

3.4. System of equations

For system of equations, a local characteristic decomposition is performed to compute the numerical flux. We refer to [18] for the details of this local characteristic decomposition and will not repeat it here. In each characteristic direction, the evaluation of the numerical flux, including the anti-diffusive sharpening procedure, is similar to the scaler case with the wind direction determined by the sign of the corresponding eigenvalue. We should emphasize that the anti-diffusive sharpening procedure may violate the entropy condition and generate entropy violating shocks when used to a non-linear characteristic field, hence in our numerical experiments we use it only in the linearly degenerate fields, for example, in the second field with eigenvalue u for the one-dimensional Euler equations.

4. Modified high order WENO finite difference scheme in two dimensions

Extension of the anti-diffusive fluxes to two dimensions is not straightforward. Many ideas of sharpening contacts, such as the artificial compression idea in [7,28] and the sub-cell resolution idea in [8], do not work as well in two dimensions. In [4], Després and Lagoutière extended their one-dimensional technique in [3] to two dimensions by dimension splitting. The adoption of dimension splitting will restrict the order of accuracy to no higher than second order. We would like to find a two-dimensional extension of the methodology which does not rely on dimensional splitting.

We will first look at the first-order case.

4.1. First-order anti-diffusive flux in two dimension

We consider a two-dimensional scalar conservation law

$$u_t + f(u)_x + g(u)_y = 0, \tag{4.1}$$

with $t > 0$, x, $y \in R$ and $f'(u) \geqslant 0$, $g'(u) \geqslant 0$. Other sign combinations of $f'(u)$ and $g'(u)$ can be handled analogously.

An explicit conservative fully discrete finite difference/finite volume scheme (again, there is no need to distinguish between them for first- and second-order schemes) has the form

$$u_{i,j}^{n+1} - u_{i,j}^n + \lambda_{i,j}^x\left(\hat{f}_{i+\frac{1}{2},j}^n - \hat{f}_{i-\frac{1}{2},j}^n\right) + \lambda_{i,j}^y\left(\hat{g}_{i,j+\frac{1}{2}}^n - \hat{g}_{i,j-\frac{1}{2}}^n\right) = 0, \tag{4.2}$$

where $u_{i,j}^n$ is the approximation either to the point value $u(x_i, y_j, t^n)$ (finite difference) or to the cell average $\frac{1}{\Delta x_i \Delta y_j}\int_{y_{j-\frac{1}{2}}}^{y_{j+\frac{1}{2}}}\int_{x_{i-\frac{1}{2}}}^{x_{i+\frac{1}{2}}} u(x, y, t^n)\,dx\,dy$ (finite volume), $\lambda_{i,j}^x = \Delta t/\Delta x_i$ and $\lambda_{i,j}^y = \Delta t/\Delta y_j$ are the local CFL numbers,

and $\hat{f}^n_{i+\frac{1}{2},j}$ and $\hat{g}^n_{i,j+\frac{1}{2}}$ are the numerical fluxes. We will again drop the superscript n which refers to the time step when there is no ambiguity. Similar to Proposition 2.1, we have the following result.

Proposition 4.1. *Assume that the CFL conditions $\lambda^x_{i,j} f'(u) \leqslant 1/d$ and $\lambda^y_{i,j} g'(u) \leqslant 1/d$ hold, where $d = 2$ is the dimension, and the numerical fluxes satisfy*

$$\hat{f}_{i+\frac{1}{2},j} \in \left[\hat{f}^{\text{diss}}_{i+\frac{1}{2},j}, \hat{f}^{\text{l}}_{i+\frac{1}{2},j}\right] \bigcap \left[\hat{f}^{\text{diss}}_{i+\frac{1}{2},j}, \hat{f}^{\text{r}}_{i+\frac{1}{2},j}\right], \tag{4.3}$$

where

$$\hat{f}^{\text{diss}}_{i+\frac{1}{2},j} = f(u_{i,j}), \quad \hat{f}^{\text{l}}_{i+\frac{1}{2},j} = \frac{u_{i,j} - u_{i-1,j}}{d\lambda^x_{i,j}} + f(u_{i-1,j}), \quad \hat{f}^{\text{r}}_{i+\frac{1}{2},j} = f(u_{i+1,j}), \tag{4.4}$$

and a symmetric condition in the y direction, then the scheme (4.2) satisfies the maximum principle

$$\min_{k,l} u^n_{k,l} \leqslant u^{n+1}_{i,j} \leqslant \max_{k,l} u^n_{k,l}. \tag{4.5}$$

Proof. Condition (4.3) allows another expression

$$\hat{f}_{i+\frac{1}{2},j} = \left(1 - \alpha^{\text{l}}_{i+\frac{1}{2},j}\right)\hat{f}^{\text{diss}}_{i+\frac{1}{2},j} + \alpha^{\text{l}}_{i+\frac{1}{2},j}\hat{f}^{\text{l}}_{i+\frac{1}{2},j}, \quad \hat{f}_{i+\frac{1}{2},j} = \left(1 - \alpha^{\text{r}}_{i+\frac{1}{2},j}\right)\hat{f}^{\text{diss}}_{i+\frac{1}{2},j} + \alpha^{\text{r}}_{i+\frac{1}{2},j}\hat{f}^{\text{r}}_{i+\frac{1}{2},j}$$

with $0 \leqslant \alpha^{\text{l}}_{i+\frac{1}{2},j},\ \alpha^{\text{r}}_{i+\frac{1}{2},j} \leqslant 1$. Similarly

$$\hat{g}_{i,j+\frac{1}{2}} = \left(1 - \beta^{\text{l}}_{i,j+\frac{1}{2}}\right)\hat{g}^{\text{diss}}_{i,j+\frac{1}{2}} + \beta^{\text{l}}_{i,j+\frac{1}{2}}\hat{g}^{\text{l}}_{i,j+\frac{1}{2}}, \quad \hat{g}_{i,j+\frac{1}{2}} = \left(1 - \beta^{\text{r}}_{i,j+\frac{1}{2}}\right)\hat{g}^{\text{diss}}_{i,j+\frac{1}{2}} + \beta^{\text{r}}_{i,j+\frac{1}{2}}\hat{g}^{\text{r}}_{i,j+\frac{1}{2}}$$

with $0 \leqslant \beta^{\text{l}}_{i,j+\frac{1}{2}}, \beta^{\text{r}}_{i,j+\frac{1}{2}} \leqslant 1$.

We can also write

$$f(u_{i,j}) - f(u_{i-1,j}) = \mu_{i-\frac{1}{2},j}(u_{i,j} - u_{i-1,j}), \quad g(u_{i,j}) - g(u_{i,j-1}) = \nu_{i,j-\frac{1}{2}}(u_{i,j} - u_{i,j-1})$$

with $\lambda^x_{i,j}\mu_{i-\frac{1}{2},j} \leqslant \frac{1}{d}$ and $\lambda^y_{i,j}\nu_{i,j-\frac{1}{2}} \leqslant \frac{1}{d}$ by the CFL conditions. Therefore, a simple manipulation gives

$$\begin{aligned}
\hat{f}_{i+\frac{1}{2},j} - \hat{f}_{i-\frac{1}{2},j} &= \left[\hat{f}^{\text{diss}}_{i+\frac{1}{2},j} + \alpha^{\text{l}}_{i+\frac{1}{2},j}\left(\hat{f}^{\text{l}}_{i+\frac{1}{2},j} - \hat{f}^{\text{diss}}_{i+\frac{1}{2},j}\right)\right] - \left[\hat{f}^{\text{diss}}_{i-\frac{1}{2},j} + \alpha^{\text{r}}_{i-\frac{1}{2},j}\left(\hat{f}^{\text{r}}_{i-\frac{1}{2},j} - \hat{f}^{\text{diss}}_{i-\frac{1}{2},j}\right)\right] \\
&= \left[\left(\frac{1}{d} - \lambda^x_{i,j}\mu_{i-\frac{1}{2},j}\right)\alpha^{\text{l}}_{i+\frac{1}{2},j} + \lambda^x_{i,j}\mu_{i-\frac{1}{2},j}\left(1 - \alpha^{\text{r}}_{i+\frac{1}{2},j}\right)\right]\frac{u_{i,j} - u_{i-1,j}}{\lambda^x_{i,j}} = C_{i,j}\frac{u_{i,j} - u_{i-1,j}}{\lambda^x_{i,j}}
\end{aligned}$$

with $0 \leqslant C_{i,j} \leqslant \frac{1}{d}$. Symmetrically we have, in the y direction

$$\begin{aligned}
\hat{g}_{i,j+\frac{1}{2}} - \hat{g}_{i,j-\frac{1}{2}} &= \left[\hat{g}^{\text{diss}}_{i,j+\frac{1}{2}} + \beta^{\text{l}}_{i,j+\frac{1}{2}}\left(\hat{g}^{\text{l}}_{i,j+\frac{1}{2}} - \hat{g}^{\text{diss}}_{i,j+\frac{1}{2}}\right)\right] - \left[\hat{g}^{\text{diss}}_{i,j-\frac{1}{2}} + \beta^{\text{r}}_{i,j-\frac{1}{2}}\left(\hat{g}^{\text{r}}_{i,j-\frac{1}{2}} - \hat{g}^{\text{diss}}_{i,j-\frac{1}{2}}\right)\right] \\
&= \left[\left(\frac{1}{d} - \lambda^y_{i,j}\nu_{i,j-\frac{1}{2}}\right)\beta^{\text{l}}_{i,j+\frac{1}{2}} + \lambda^y_{i,j}\nu_{i,j-\frac{1}{2}}\left(1 - \beta^{\text{r}}_{i,j+\frac{1}{2}}\right)\right]\frac{u_{i,j} - u_{i,j-1}}{\lambda^y_{i,j}} = D_{i,j}\frac{u_{i,j} - u_{i,j-1}}{\lambda^y_{i,j}}
\end{aligned}$$

with $0 \leqslant D_{i,j} \leqslant \frac{1}{d}$. Now the scheme (4.2) becomes

$$u^{n+1}_{i,j} = u^n_{i,j} - C_{i,j}(u^n_{i,j} - u^n_{i-1,j}) - D_{i,j}(u^n_{i,j} - u^n_{i,j-1}) = (1 - C_{i,j} - D_{i,j})u^n_{i,j} + C_{i,j}u^n_{i-1,j} + D_{i,j}u^n_{i,j-1}. \tag{4.6}$$

Since $C_{i,j} \geqslant 0$, $D_{i,j} \geqslant 0$ and $C_{i,j} + D_{i,j} \leqslant \frac{1}{d} + \frac{1}{d} = 1$, the right-hand side of (4.6) is a convex combination of $u^n_{i,j}$, $u^n_{i-1,j}$ and $u^n_{i,j-1}$. Therefore, the maximum principle (4.5) holds. □

We now define the limited downwind flux in the two-dimensional case.

Definition 4.2. The limited downwind flux $\hat{f}^{\text{a}}_{i+\frac{1}{2},j}$ in the two-dimensional case is defined by

$$\left[\hat{f}^{\text{diss}}_{i+\frac{1}{2},j}, \hat{f}^{\text{l}}_{i+\frac{1}{2},j}\right] \bigcap \left[\hat{f}^{\text{diss}}_{i+\frac{1}{2},j}, \hat{f}^{\text{r}}_{i+\frac{1}{2},j}\right] = \left[\hat{f}^{\text{diss}}_{i+\frac{1}{2},j}, \hat{f}^{\text{a}}_{i+\frac{1}{2},j}\right], \tag{4.7}$$

where $\hat{f}^{\text{diss}}_{i+\frac{1}{2},j}$, $\hat{f}^{\text{l}}_{i+\frac{1}{2},j}$ and $\hat{f}^{\text{r}}_{i+\frac{1}{2},j}$ are defined in (4.4). An equivalent form of this limited downwind flux is

$$\hat{f}^{\text{a}}_{i+\frac{1}{2},j} = f(u_{i,j}) + \text{minmod}\left(\frac{u_{i,j} - u_{i-1,j}}{d\lambda^x_{i,j}} + f(u_{i-1,j}) - f(u_{i,j}), f(u_{i+1,j}) - f(u_{i,j})\right). \tag{4.8}$$

The definition of $\hat{g}^{\text{a}}_{i,j+\frac{1}{2}}$ is symmetric.

From Proposition 4.1, we know that scheme (4.2) with the flux (4.8) satisfies the maximum principle. However, we cannot prove that it is TVD. We will perform a numerical test to see the behavior of this scheme. The numerical test will be performed on the two-dimensional linear advection equation

$$u_t + u_x + u_y = 0, \tag{4.9}$$

defined on $-1 \leqslant x < 1$, $-1 \leqslant y < 1$, with the following initial conditions:

$$u(x,y,0) = \begin{cases} 1, & |x| \leqslant 0.5, \ |y| \leqslant 0.5, \\ 0, & \text{otherwise}, \end{cases} \quad \text{or} \quad u(x,y,0) = \begin{cases} 1, & x^2 + y^2 \leqslant 0.5, \\ 0, & \text{otherwise}, \end{cases} \tag{4.10}$$

and periodic boundary conditions. We run the scheme up to $t = 20$, namely 10 periods later. The results are plotted in Fig. 1. Clearly, the results are not satisfactory and do not seem to be TVD. The problem might be related to the linear instability with the explicit Euler forward time discretization, as too much of the downwind information is used in the flux (4.8). A related phenomenon is the well-known result of Goodman and LeVeque [6] that no second or higher order TVD schemes exist in two dimensions.

If we use instead a second or higher order TVD Runge–Kutta time discretization with the same anti-diffusive flux (4.8), the results look very different and much better, see Fig. 2. Similar to the one-dimensional case, the scheme is able to maintain sharp contact discontinuities for very long time without progressively more severe smearing. As we know, central difference with first-order Euler forward time discretization is linearly unconditionally unstable for the linear advection equation (4.9), while central difference with third or higher order Runge–Kutta time discretization is linearly stable under suitable CFL conditions. The

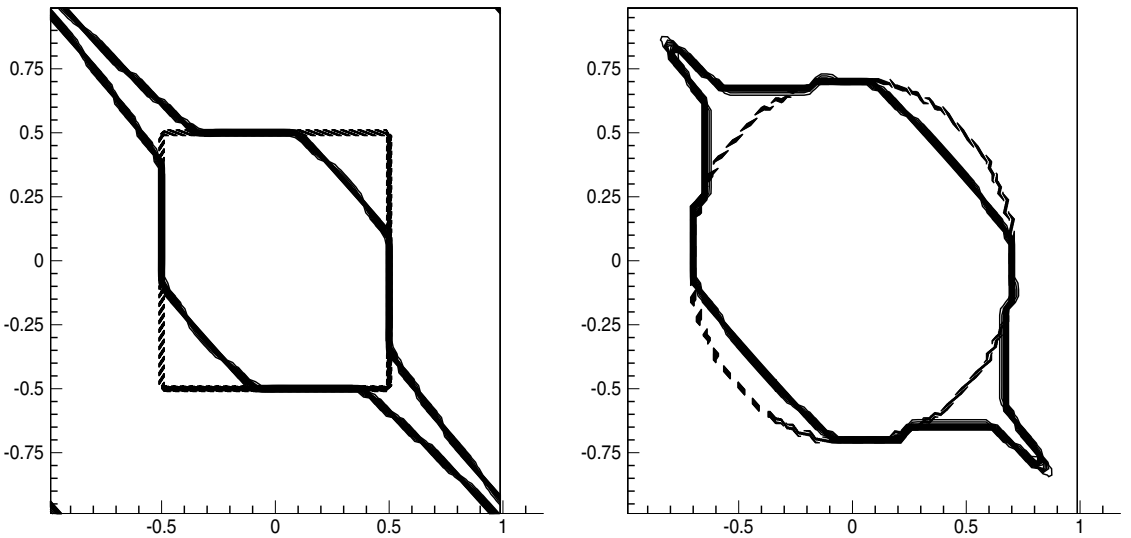

Fig. 1. 80×80 uniform mesh. CFL = 0.3. Euler forward in time. Dashed lines: the exact solution (10 equally spaced contours from 0 to 1); solid lines: the numerical solution (10 equally spaced contours from 0 to 1).

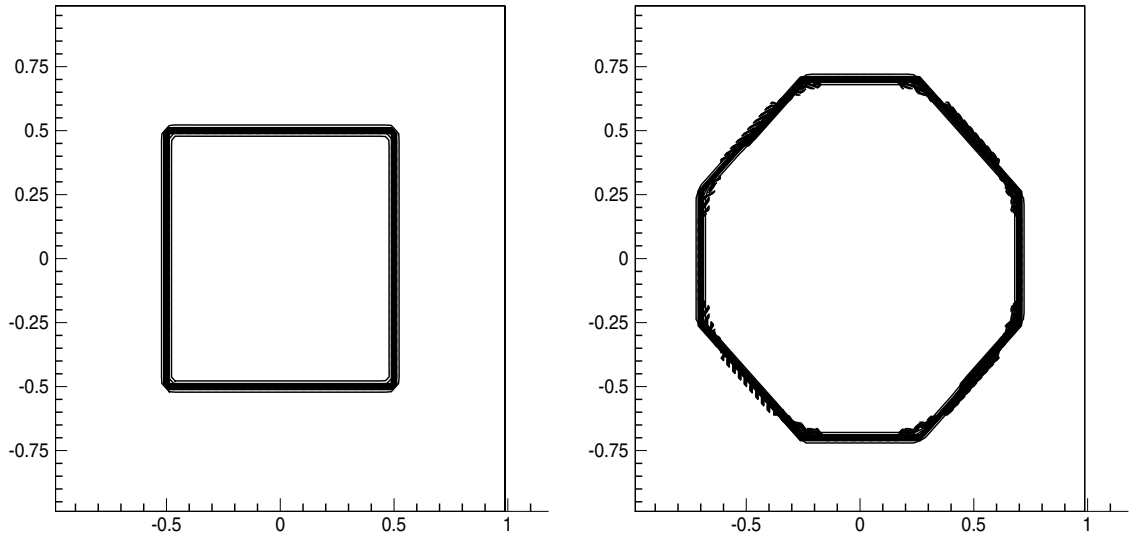

Fig. 2. 80×80 uniform mesh. CFL = 0.3. Second-order Runge–Kutta in time. Dashed lines: the exact solution (10 equally spaced contours from 0 to 1); solid lines: the numerical solution (10 equally spaced contours from 0 to 1).

comparison of the results in Figs. 1 and 2 strongly suggests that linear instability is the cause of the bad behavior of the scheme (4.2) with the flux (4.8) when first-order Euler forward time discretization is used. One must use at least a second-order Runge–Kutta time discretization.

We now generalize the first-order anti-diffusive scheme to higher order WENO finite difference schemes.

4.2. Anti-diffusive fluxes with high order WENO finite difference reconstruction in two dimension

Two-dimensional finite difference WENO schemes [11] are similar to that for one dimension, with numerical fluxes computed in each direction. Thus, when the usual WENO fluxes $\hat{f}^{\pm}_{i+\frac{1}{2},j}$ are computed, we obtain the anti-diffusive fluxes by

$$\hat{f}^{\mathrm{a}}_{i+\frac{1}{2},j} = \hat{f}^{-}_{i+\frac{1}{2},j} + \varphi_{i,j}\mathrm{minmod}\left(\frac{u_{i,j}-u_{i-1,j}}{d\lambda^{x}_{i,j}} + \hat{f}^{-}_{i-\frac{1}{2},j} - \hat{f}^{-}_{i+\frac{1}{2},j}, \hat{f}^{+}_{i+\frac{1}{2},j} - \hat{f}^{-}_{i+\frac{1}{2},j}\right).$$

For fixed j, $\varphi_{i,j}$ has the same definition as (3.14) in one dimension. Symmetrically for the y direction, we have

$$\hat{g}^{\mathrm{a}}_{i,j+\frac{1}{2}} = \hat{g}^{-}_{i,j+\frac{1}{2}} + \psi_{i,j}\mathrm{minmod}\left(\frac{u_{i,j}-u_{i,j-1}}{d\lambda^{y}_{i,j}} + \hat{g}^{-}_{i,j-\frac{1}{2}} - \hat{g}^{-}_{i,j+\frac{1}{2}}, \hat{g}^{+}_{i,j+\frac{1}{2}} - \hat{g}^{-}_{i,j+\frac{1}{2}}\right)$$

with the discontinuity indicator $\psi_{i,j}$ defined similarly to (3.14) in the y direction with fixed x_i.

We use the third-order TVD Runge–Kutta method (3.10) for the time discretization.

Two-dimensional systems are treated dimension by dimension, with each dimension dealt with the procedure described in Section 3.4.

5. Numerical results

In this section, we provide numerical results to demonstrate the behavior of the anti-diffusive high order WENO finite difference schemes. We use the fifth-order WENO scheme in [11], based on the Lax–Friedrichs

flux splitting and the local characteristic decomposition for the system case, as our base scheme. The CFL number is taken as 0.3, except for the accuracy tests where the CFL numbers are taken smaller for more refined meshes to guarantee that spatial errors dominate.

5.1. One-dimensional scalar linear equations

In this section, we test our schemes on one-dimensional scalar linear problems. The computational domain is $-1 < x \leqslant 1$ and periodic boundary conditions are used for all problems in this section.

Example 5.1. We test the accuracy of the anti-diffusive fifth-order WENO finite difference scheme for the linear advection equation

$$u_t + u_x = 0 \tag{5.1}$$

with the initial condition

$$u(x,0) = \sin(\pi x),$$

up to $t = 2$. The results and a comparison with the original fifth-order WENO scheme [11] are given in Table 1. We can clearly see that fifth-order accuracy is achieved and the errors of the fifth-order anti-diffusive WENO scheme are comparable with that of the original fifth-order WENO scheme.

Example 5.2. We solve the linear advection equation (5.1) with the initial condition

$$u(x,0) = \begin{cases} 1, & -0.5 < x \leqslant 0.5, \\ 0, & \text{otherwise.} \end{cases} \tag{5.2}$$

The results at $t = 10$ (after five-time periods) and at $t = 100$ (after 50-time periods) are shown in Fig. 3. We can see clearly that the regular fifth-order WENO scheme progressively smears the contact discontinuities more severely with larger time, while the anti-diffusive fifth-order WENO scheme has a sharp resolution for the contacts which does not deteriorate noticeably with larger time.

Example 5.3. We solve the linear advection equation (5.1) with the following initial condition:

$$u(x,0) = \begin{cases} -x\sin\left(\frac{3\pi}{2}x^2\right), & -1 < x \leqslant -\frac{1}{3}, \\ |\sin(2\pi x)|, & -\frac{1}{3} < x \leqslant \frac{1}{3}, \\ 2x - 1 - \frac{1}{6}\sin(3\pi x), & \frac{1}{3} \leqslant x \leqslant 1. \end{cases}$$

The solution of this problem contains both contact discontinuities and corner singularities (discontinuities in the first derivative), and smooth structures. The results at $t = 11$ (after 5.5-time periods) and at $t = 101$ (after 50.5-time periods) are shown in Fig. 4. We can again see that the regular fifth-order WENO scheme

Table 1
Errors and numerical orders of accuracy of the fifth-order anti-diffusive WENO scheme and the original fifth-order WENO scheme for the one-dimensional linear advection equation (5.1)

N	Anti-diffusive WENO				Original WENO			
	L^1 error	Order	L^∞ error	Order	L^1 error	Order	L^∞ error	Order
40	3.75E − 5		8.70E − 5		4.47E − 5		8.82E − 5	
80	1.32E − 6	4.82	2.88E − 6	4.91	1.39E − 6	5.00	2.83E − 6	4.96
160	4.30E − 8	5.00	8.63E − 8	5.04	4.36E − 8	5.00	8.51E − 8	5.05
320	1.35E − 9	5.00	2.55E − 9	5.07	1.36E − 9	5.00	2.55E − 9	5.06
640	4.21E − 11	5.01	7.31E − 11	5.12	4.22E − 11	5.01	7.32E − 11	5.12

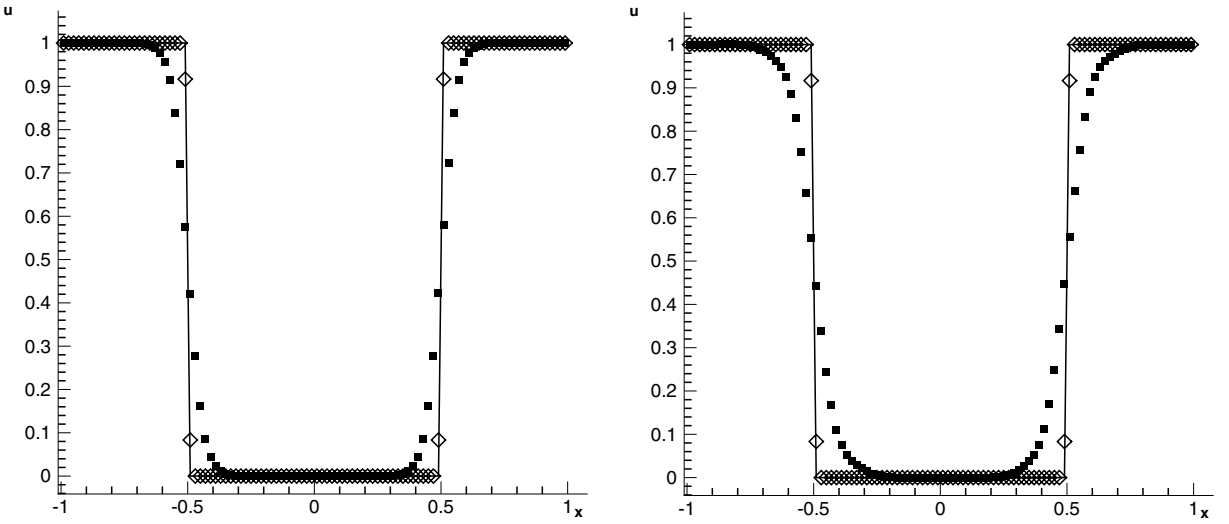

Fig. 3. Example 5.2. One-dimensional linear advection. 100 uniform mesh points. Solid lines: the exact solution; solid rectangle symbols: numerical solution of the regular fifth-order WENO scheme; unfilled diamond symbols: numerical solution of the anti-diffusive fifth-order WENO scheme. Left: $t = 10$; right: $t = 100$.

progressively smears the contact discontinuities more severely with larger time, while the anti-diffusive fifth-order WENO scheme has a sharp resolution for the contacts which does not deteriorate noticeably with larger time.

Example 5.4. We solve the variable coefficient linear equation

$$u_t + ((2 + \sin(\pi(x+1)))u)_x = 0$$

with the initial condition (5.2). The results at $t = 10$ and at $t = 100$ are shown in Fig. 5. We can again observe a significant improvement of the anti-diffusive fifth-order WENO scheme over the regular fifth-order WENO scheme in the resolution of the contact discontinuities, especially for larger time.

5.2. One-dimensional systems

In this section, we test our schemes on the one-dimensional Euler equations of compressible gas dynamics

$$\mathbf{u}_t + \mathbf{f}(\mathbf{u})_x = 0,$$

here $\mathbf{u} = (\rho, \rho u, E)$, $\mathbf{f}(\mathbf{u}) = (\rho u, \rho u^2 + p, u(E + p))$, where ρ is the density, u is the velocity, E is the total energy and $p = (\gamma - 1)\left(E - \frac{1}{2}\rho u^2\right)$ is the pressure. γ is the gas constant which is taken as 1.4 in our numerical tests.

As explained in Section 3.4, the anti-diffusive flux is used only in the linearly degenerate second field, with the eigenvalue u. The usual Lax–Friedrichs flux splitting [11] is used in the genuinely non-linear first and third characteristic fields.

Example 5.5. We solve the one-dimensional shock-tube problem of Sod [23], with the initial condition

$$\mathbf{u}(x,0) = \begin{cases} \rho = 1.0, \ u = 0.0, \ p = 1.0, & 0 < x < 0.5, \\ \rho = 0.125, \ u = 0.0, \ p = 0.1, & 0.5 \leqslant x < 1, \end{cases}$$

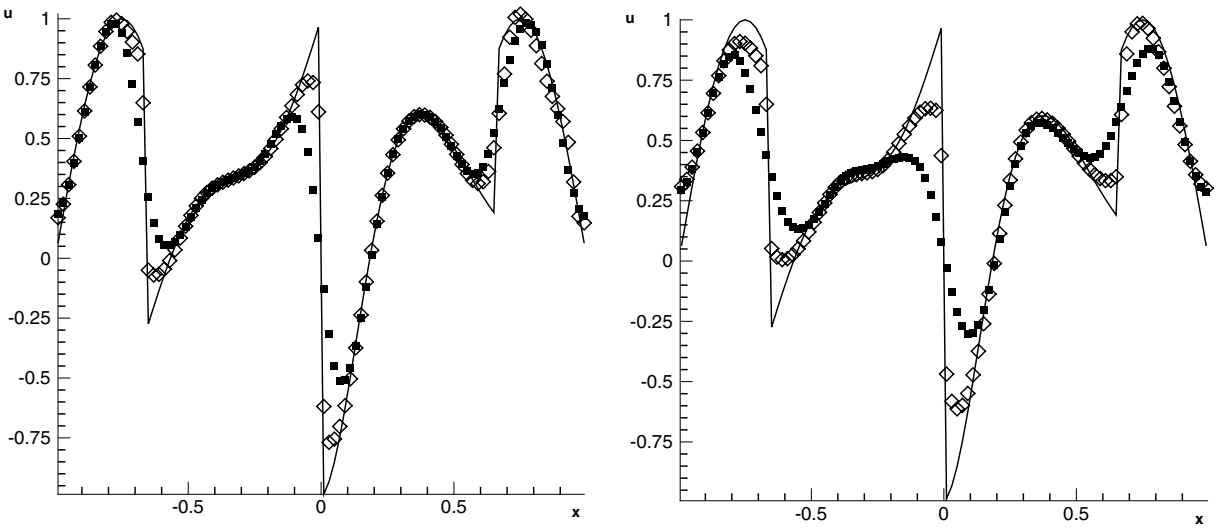

Fig. 4. Example 5.3. One-dimensional linear advection. 100 uniform mesh points. Solid lines: the exact solution; solid rectangle symbols: numerical solution of the regular fifth-order WENO scheme; unfilled diamond symbols: numerical solution of the anti-diffusive fifth-order WENO scheme. Left: $t = 11$; right: $t = 101$.

The density ρ at $t = 0.14$ is plotted in Fig. 6. We can observe a significant improvement of the anti-diffusive fifth-order WENO scheme over the regular fifth-order WENO scheme in the resolution of the contact discontinuity. This improvement can be seen more clearly in the zoomed picture on the right of Fig. 6.

Example 5.6. We solve the one-dimensional shock-tube problem of Lax [12] with the initial condition

$$\mathbf{u}(x,0) = \begin{cases} \rho = 0.445, \ u = 0.698, \ p = 3.528, & 0 < x < 0.5, \\ \rho = 0.5, \ u = 0.0, \ p = 0.571, & 0.5 \leqslant x < 1. \end{cases}$$

The density ρ at $t = 0.17$ is plotted in Fig. 7. We can again observe a significant improvement of the anti-diffusive fifth-order WENO scheme over the regular fifth-order WENO scheme in the resolution of the contact discontinuity, in the sense that the number of transition points for the contact discontinuity is significantly reduced by the anti-diffusive procedure.

Example 5.7. In this example, we solve the problem of two interactive blast waves [27]. The initial condition is given as

$$\mathbf{u}(x,0) = \begin{cases} \mathbf{u}_{\mathrm{L}}, & 0 < x < 0.1, \\ \mathbf{u}_{\mathrm{M}}, & 0.1 < x < 0.9, \\ \mathbf{u}_{\mathrm{R}}, & 0.9 < x < 1, \end{cases}$$

where $\rho_{\mathrm{L}} = \rho_{\mathrm{M}} = \rho_{\mathrm{R}} = 1$, $u_{\mathrm{L}} = u_{\mathrm{M}} = u_{\mathrm{R}} = 0$, $p_{\mathrm{L}} = 10^3$, $p_{\mathrm{M}} = 10^{-2}$ and $p_{\mathrm{R}} = 10^2$. Reflective boundary conditions are applied at both $x = 0$ and $x = 1$. The results for the density ρ at $t = 0.038$ are plotted in Fig. 8. We can clearly see a significant improvement of the anti-diffusive fifth-order WENO scheme over the regular fifth-order WENO scheme in the resolution of the contact discontinuities.

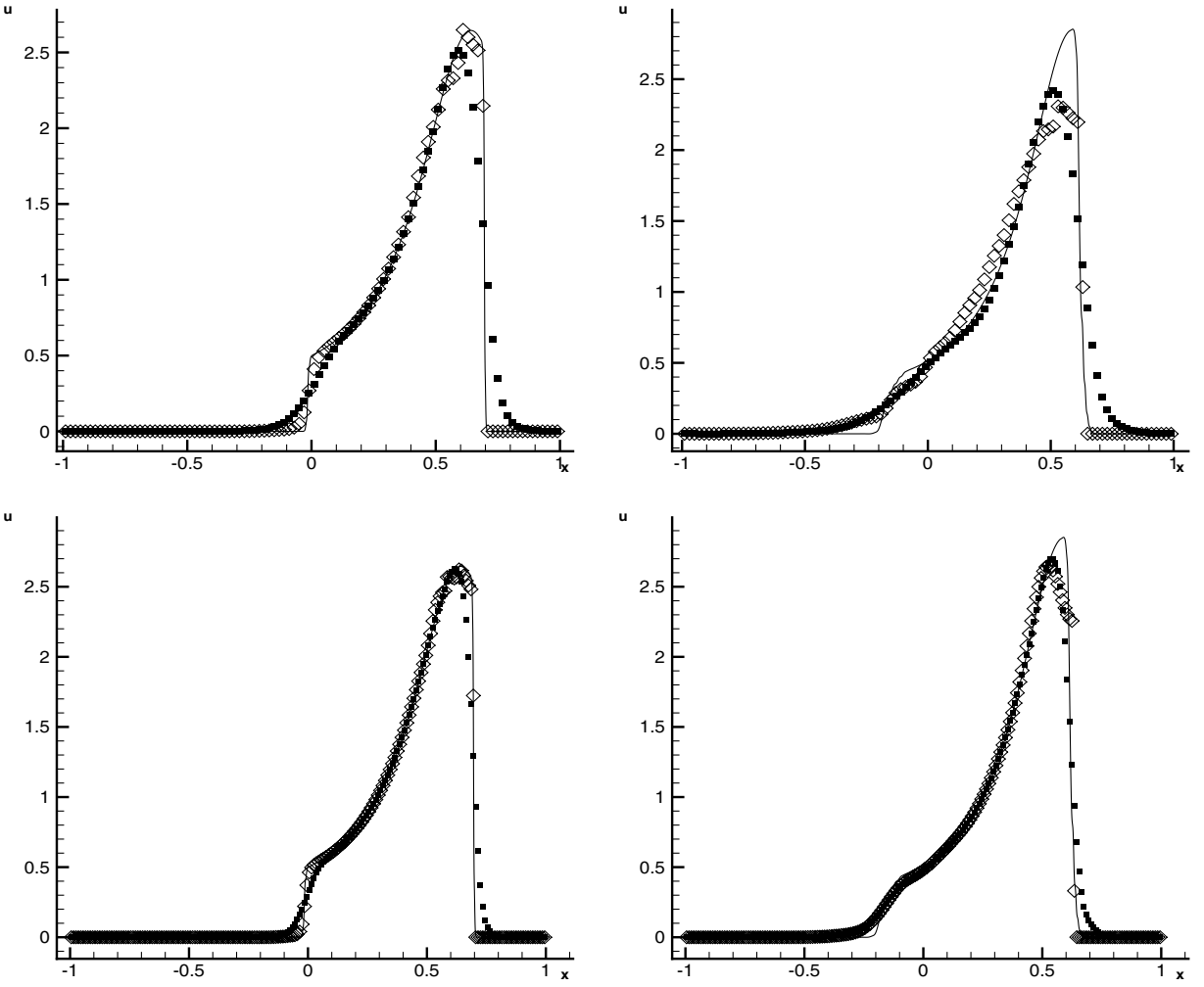

Fig. 5. Example 5.4. One-dimensional linear equation with variable coefficient. Top to bottom: 100 and 200 uniform mesh points. Solid lines: the exact solution; solid rectangle symbols: numerical solution of the regular fifth-order WENO scheme; unfilled diamond symbols: numerical solution of the anti-diffusive fifth-order WENO scheme. Left: $t = 10$; right: $t = 100$.

5.3. Two-dimensional scalar linear equations

In this section, we test our schemes on two-dimensional scalar linear equations. The computational domain is $(x, y) \in [-1, 1]^2$ with periodic boundary conditions.

Example 5.8. We solve the two-dimensional advection equation (4.9) with the two initial conditions given by (4.10). The results at $t = 40$ (after 20-time periods) are given in Figs. 9 and 10. We can observe a significant improvement of the anti-diffusive fifth-order WENO scheme over the regular fifth-order WENO scheme in the resolution of the contact discontinuities, especially for longer time. Notice that the contours of the exact solution and the anti-diffusive numerical solution for the disk case (Fig. 10, bottom right) are very close to each other, indicating that the numerical solution maintains the shape quite well, even though it looks like a polygon in Fig. 9, bottom right, due to a visual deception.

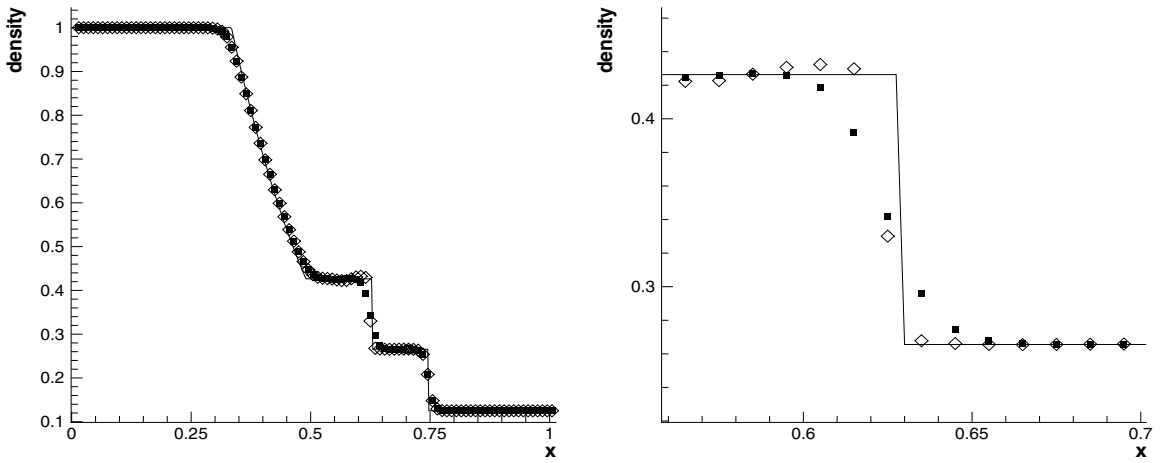

Fig. 6. Example 5.5. One-dimensional Euler equations. Sod's shock tube problem. Density ρ. 100 uniform mesh points. $t = 0.14$. Solid line: the exact solution; solid rectangle symbols: numerical solution of the regular fifth-order WENO scheme; unfilled diamond symbols: numerical solution of the anti-diffusive fifth-order WENO scheme. Left: the whole domain; right: zoom around the contact discontinuity.

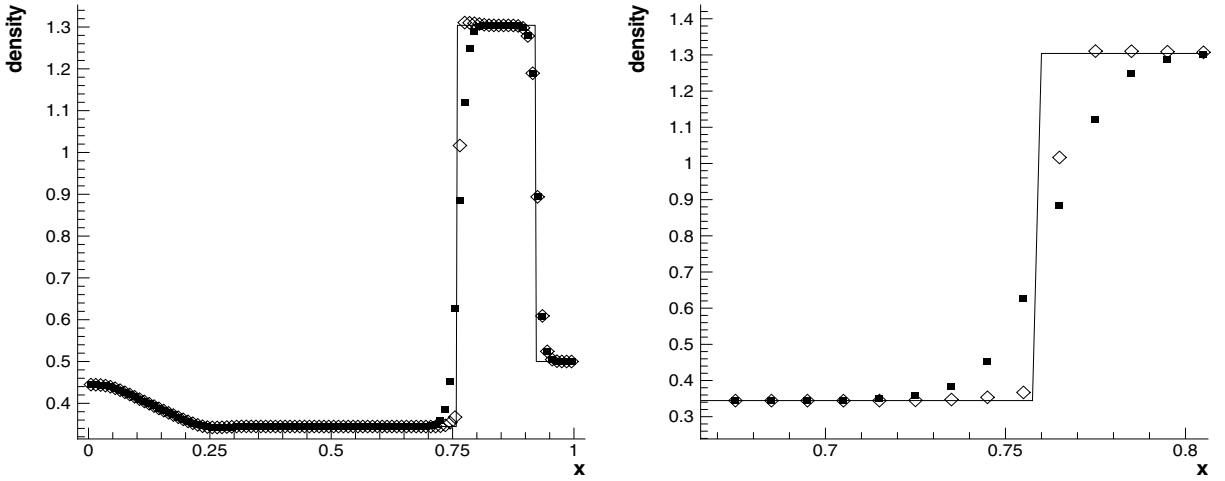

Fig. 7. Example 5.6. One-dimensional Euler equations. Lax's shock tube problem. Density ρ. 100 uniform mesh points. $t = 0.17$. Solid line: the exact solution; solid rectangle symbols: numerical solution of the regular fifth-order WENO scheme; unfilled diamond symbols: numerical solution of the anti-diffusive fifth-order WENO scheme. Left: the whole domain; right: zoom around the contact discontinuity.

Example 5.9. We solve the two-dimensional linear advection equation with variable coefficients

$$u_t - yu_x + xu_y = 0 \tag{5.3}$$

with an initial condition

$$u(x,y,0) = \begin{cases} 1, & (x+0.4)^2 + (y+0.4)^2 \leqslant 0.09, \\ 0, & \text{otherwise.} \end{cases} \tag{5.4}$$

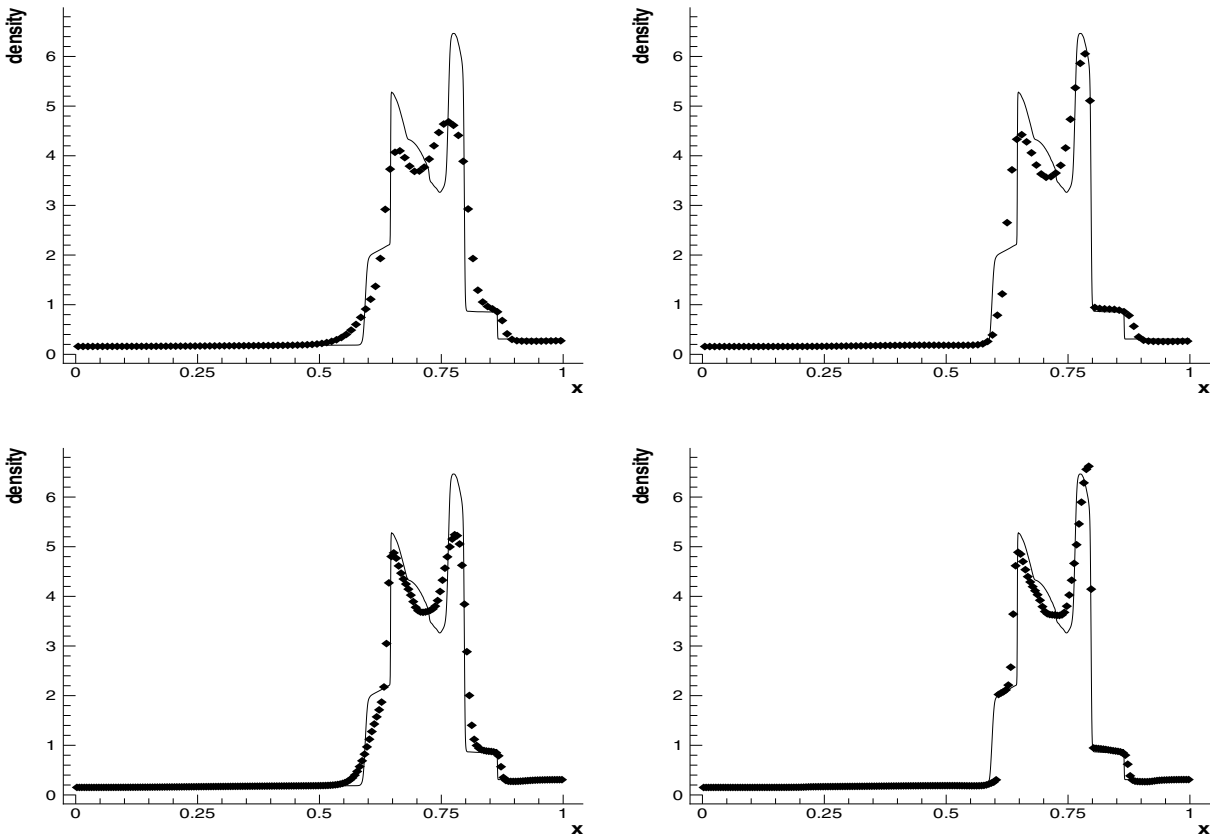

Fig. 8. Example 5.7. Blast wave problem. Density ρ. $t = 0.038$. CFL = 0.3. Solid line: the reference solution computed with 2000 uniform mesh points using the regular fifth-order WENO scheme; Symbols: the numerical solutions. Top: 100 uniform mesh points; bottom: 200 uniform mesh points. $t = 0.038$. Left: results of the regular fifth-order WENO scheme; right: the results of the anti-diffusive fifth-order WENO scheme.

This is a solid body rotation around origin. The computational result at $t = 2\pi$ (after one rotation) is given in Fig. 11. We can again observe a significant improvement of the anti-diffusive fifth-order WENO scheme over the regular fifth-order WENO scheme in the resolution of the contact discontinuity.

5.4. Two-dimensional systems

In this section, we test our schemes on the two-dimensional Euler equations of compressible gas dynamics

$$\mathbf{u}_t + \mathbf{f}(\mathbf{u})_x + \mathbf{g}(\mathbf{u})_y = 0, \tag{5.5}$$

where $\mathbf{u} = (\rho, \rho u, \rho v, E)$, $\mathbf{f}(\mathbf{u}) = (\rho u, \rho u^2 + p, \rho uv, u(E + p))$, $\mathbf{g}(\mathbf{u}) = (\rho v, \rho vu, \rho v^2 + p, v(E + p))$, and again ρ is the density, (u,v) is the velocity, E is the total energy and $p = (\gamma - 1)(E - \frac{1}{2}(\rho u^2 + \rho v^2))$ is the pressure. γ is the gas constant which is again taken as 1.4 in our numerical tests, unless otherwise stated.

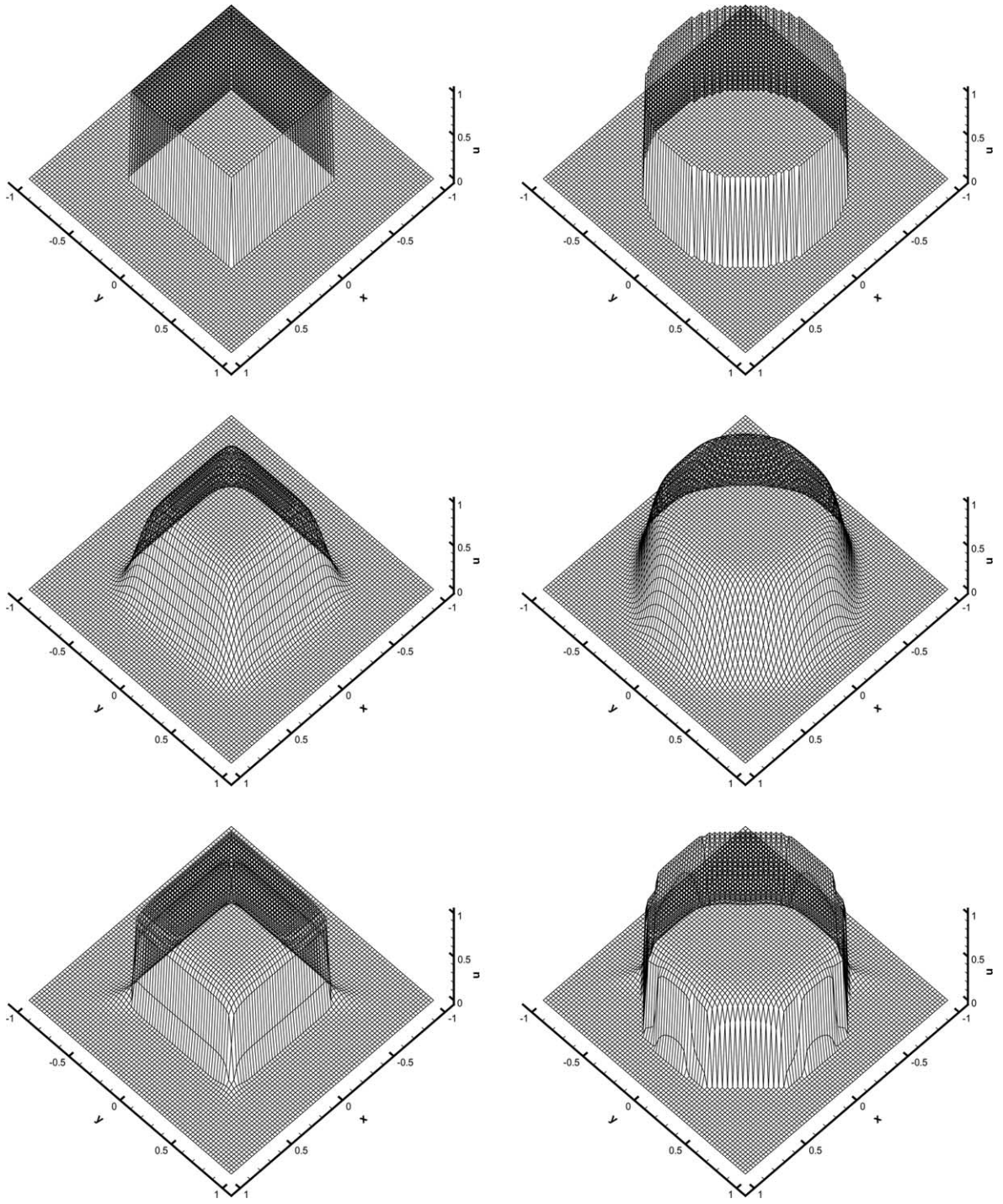

Fig. 9. Example 5.8. Linear advection. 80×80 uniform mesh. $t = 40$. Left: the square initial condition; right: the circular initial condition. Top: the exact solution; middle: the regular fifth-order WENO scheme; bottom: the anti-diffusive fifth-order WENO scheme.

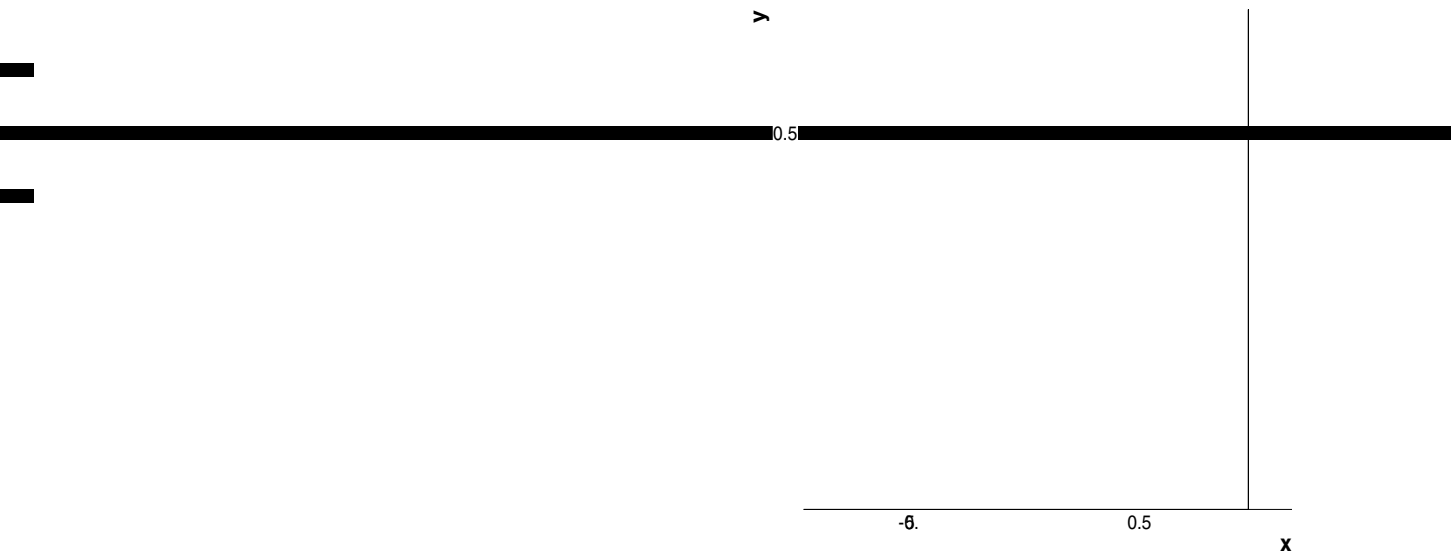
y
0.5
-6.
0.5
x

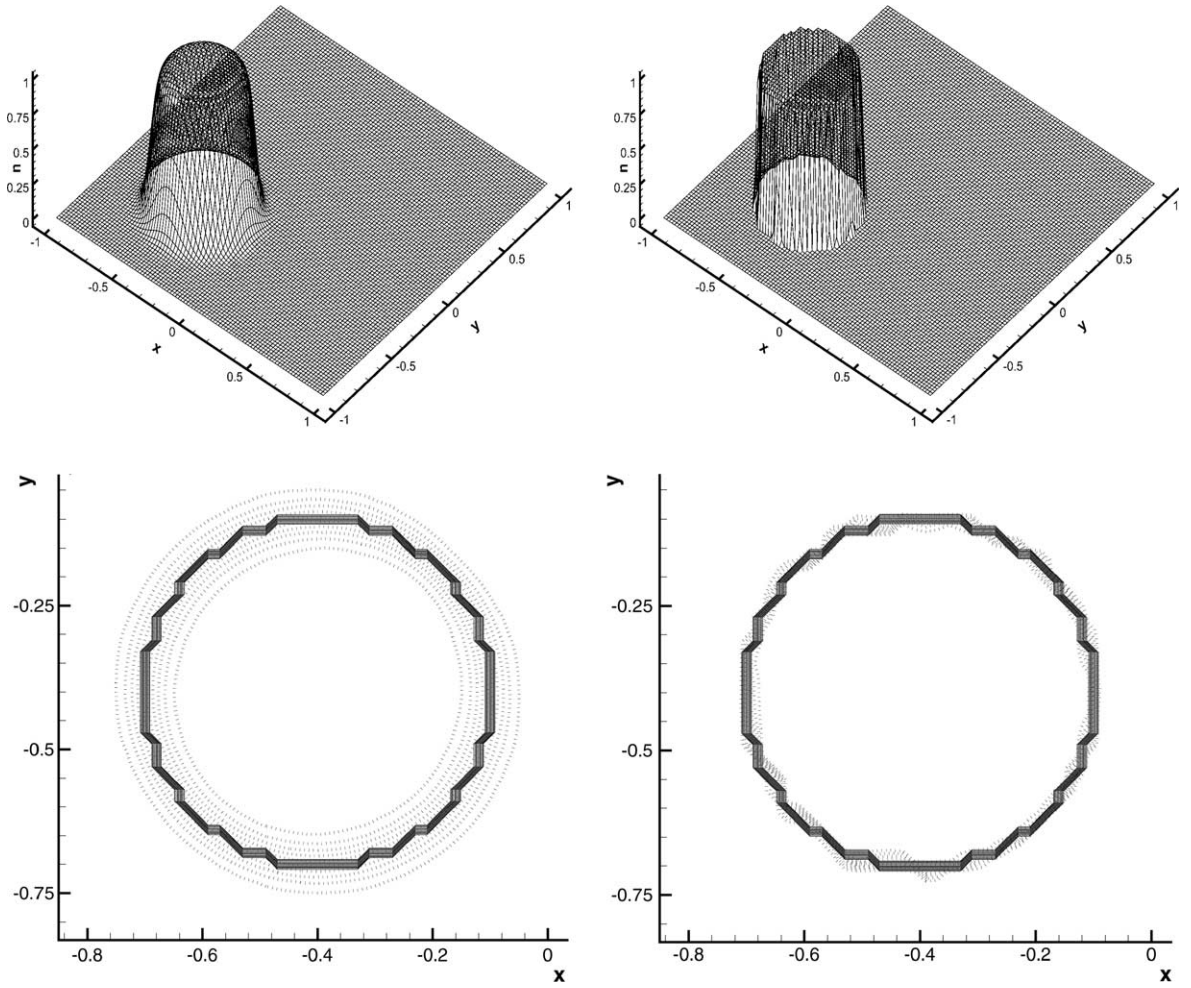

Fig. 11. Example 5.9. Linear equation with variable coefficients (5.3). Solid body rotation. 100×100 uniform mesh. $t = 2\pi$. Top: surface; bottom: 10 equally distributed contours from 0 to 1.0 in a zoomed region. Left: the regular fifth-order WENO scheme; right: the anti-diffusive fifth-order WENO scheme.

$\rho(x, y, t) = 1 + 0.2\sin(\pi(x + y - 0.5t))$, and u, v and p will remain as constants. The results and a comparison with the original fifth-order WENO scheme [11] are given in Table 2. We can clearly see that fifth-order accuracy is achieved and the errors of the fifth-order anti-diffusive WENO scheme are comparable with that of the original fifth-order WENO scheme.

Example 5.11. We solve the two-dimensional Euler equation (5.5) with an initial condition $\rho = 2$, $p = 1$, $u = v = 1$ when $(x - 0.5)^2 + (y - 0.5)^2 \leqslant 0.09$, and $\rho = 1, p = 1, u = v = 1$ outside this circle. This is a moving cylinder. The results at $t = 2$ (after two-time periods) and at $t = 20$ (after 20-time periods) are given in Figs. 12 and 13. We can again observe a significant improvement of the anti-diffusive fifth-order WENO scheme over the regular fifth-order WENO scheme in the resolution of the contact discontinuities, especially for longer time.

Table 2
Errors and numerical orders of accuracy of the fifth-order anti-diffusive WENO scheme and the original fifth-order WENO scheme for the two-dimensional Euler equation (5.5)

$N_x \times N_y$	Anti-diffusive WENO				Original WENO			
	L^1 error	Order	L^∞ error	Order	L^1 error	Order	L^∞ error	Order
40×40	3.23E − 6		6.87E − 6		3.48E − 6		7.08E − 6	
80×80	1.01E − 7	4.99	2.03E − 7	5.05	1.09E − 7	5.00	2.13E − 7	5.05
160×160	3.14E − 9	5.01	5.51E − 9	5.20	3.35E − 9	5.02	5.90E − 9	5.17
320×320	9.20E − 11	5.09	1.53E − 10	5.17	9.82E − 11	5.09	1.63E − 10	5.18
640×640	2.54E − 12	5.17	5.48E − 12	4.80	2.72E − 12	5.17	5.78E − 12	4.82

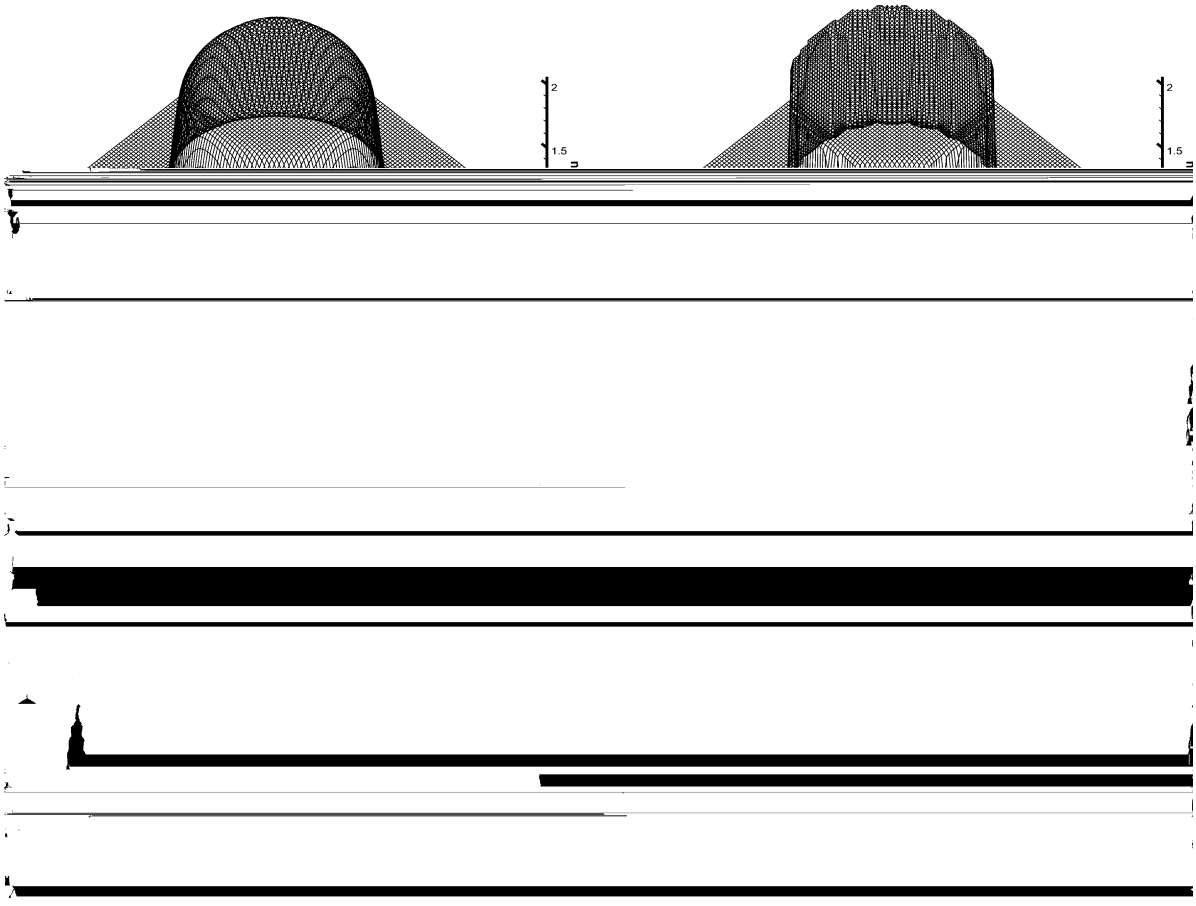

Fig. 12. Example 5.11. Moving cylinder. Two-dimensional Euler equations. 100×100 uniform mesh. Top: $t = 2$; bottom: $t = 20$. Left: the regular fifth-order WENO scheme; right: the anti-diffusive fifth-order WENO scheme.

Example 5.12. *Raleigh–Taylor instability*. Rayleigh–Taylor instability happens on an interface between fluids with different densities when an acceleration is directed from heavy fluid to light one. This problem has been simulated extensively in the literature, e.g. [5] and [29]. The problem is set up as follows: the computational domain is $[0, 1/4] \times [0, 1]$. Initially, the interface is at $y = 1/2$, the heavy fluid with $\rho = 2$ is below the interface, and the light fluid with density $\rho = 1$ is above the interface with gravity acceleration in the positive

regular fifth-order WENO scheme [17] is given in Fig. 14. The results using the anti-diffusive fifth-order WENO scheme is shown in Fig. 15. We can clearly see that the contact discontinuity resolution (manifested by the small scale structures) is significantly improved by the anti-diffusive modification to the fifth-order WENO scheme. We remark that, as pointed out in [17,30], since we have used the inviscid Euler equations, the details of the complex solution structures due to the physical instability of contact discontinuities are related to the specific form of numerical viscosity of the scheme. A physically correct calculation for these problems would have to use the Navier–Stokes equations with the real physical viscosity [30]. However, the

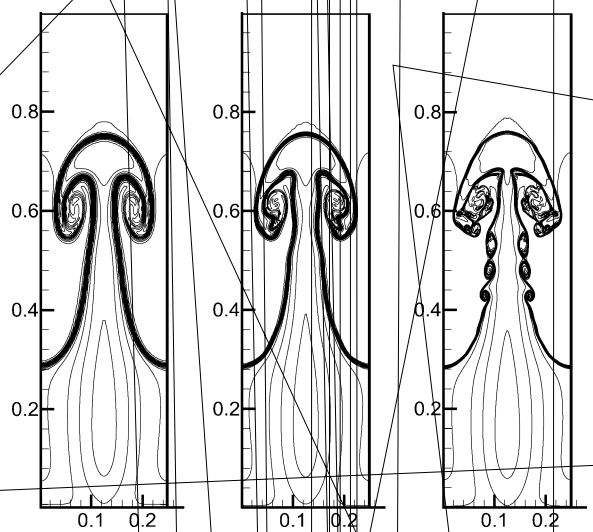

Fig. 14. Raleigh–Taylor instability problem. Density at $t = 1.95$. Regular fifth-order WENO scheme. $\Delta x = \Delta y = 1/240$ (left), 1/480 (middle) and 1/960 (right). 15 equally spaced contours from $\rho = 0.952269$ to $\rho = 2.14589$.

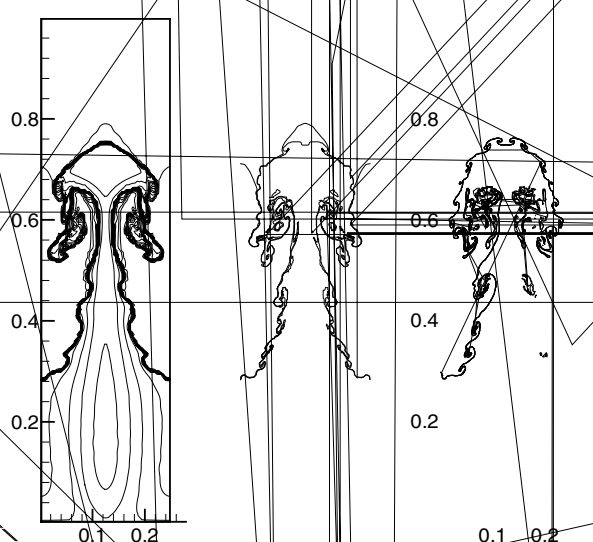

Fig. 15. Raleigh–Taylor instability problem. Density at $t = 1.95$. The anti-diffusive fifth-order WENO scheme. $\Delta x = \Delta y = 1/240$ (left), 1/480 (middle) and 1/960 (right). 15 equally spaced contours from $\rho = 0.952269$ to $\rho = 2.14589$.

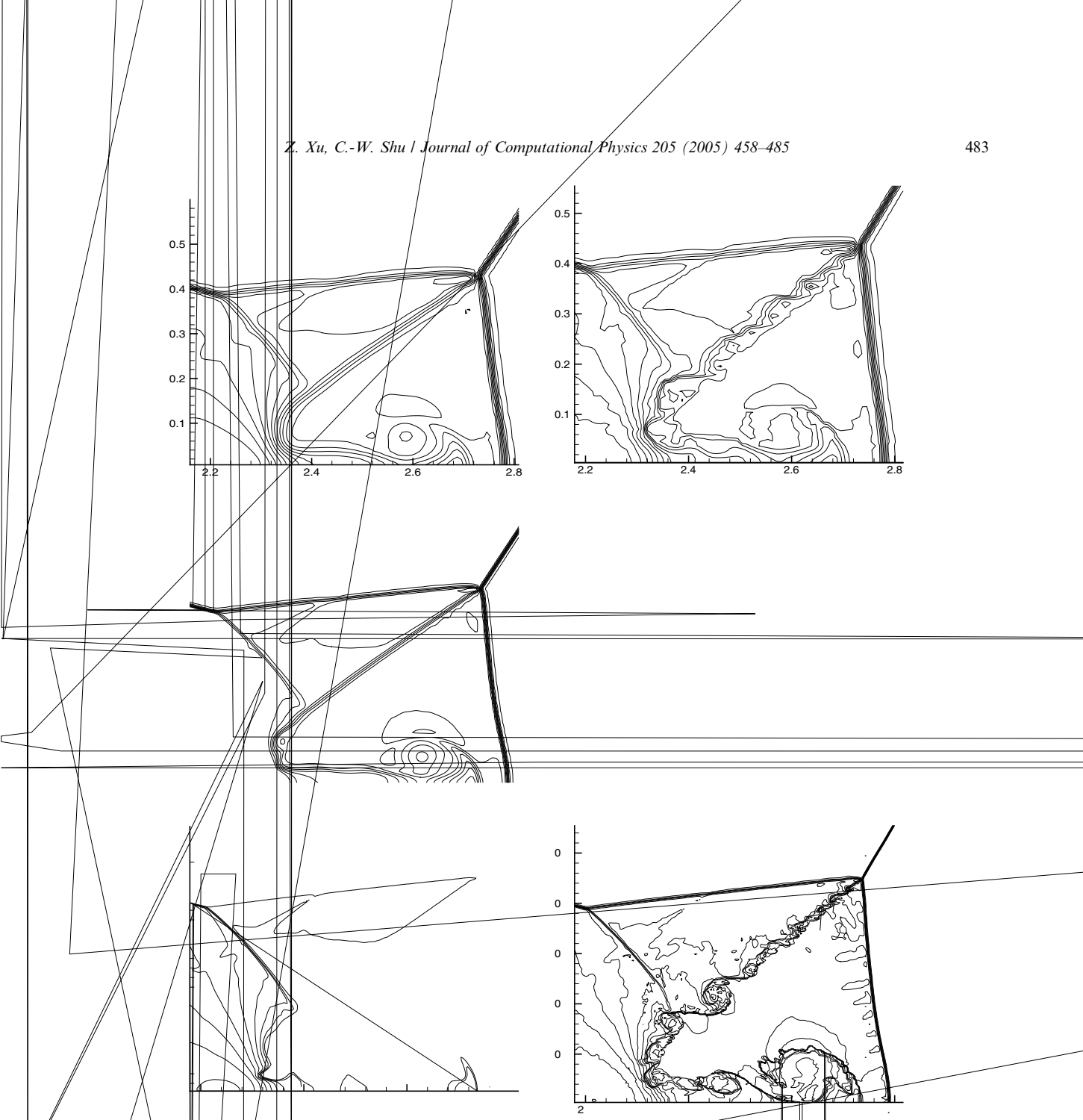

Fig. 17. Double Mach reflection problem. Density at $t = 0.2$. 30 equally spaced contours from $\rho = 1.5$ to $\rho = 22.9705$. From top to bottom: $\Delta x = \Delta y = 1/120$, 1/240 and 1/480. Left: regular fifth-order WENO scheme; right: the anti-diffusive fifth-order WENO scheme.

This problem contains a strong shock, near which the anti-diffusive fluxes should not be used. We apply an ad hoc pressure based criterion, originally proposed in [14], to switch between a regular Lax–Friedrichs based WENO flux and a anti-diffusive WENO flux. Specifically, when evaluating the flux in the x direction, we compute a normalized pressure jump $S_{i,j} = \frac{|p_{i-1,j-1}-p_{i,j+1}|+|p_{i-1,j+1}-p_{i,j-1}|}{\min(|p_{i-1,j-1}|,|p_{i,j+1}|,|p_{i-1,j+1}|,|p_{i,j-1}|)}$. If $S_{i,j} > 10$, we use the original

LaxFriedrichs based WENO flux for the linearly degenerate fields, otherwise we use anti-diffusive WENO flux. The procedure is adopted for the flux in the y direction symmetrically. Notice that the threshold $S_{i,j} > 10$ is not generic and might need to be adjusted for different problems.

The simulation results using the regular fifth-order WENO scheme [11] is given in Fig. 16, left. The results using the anti-diffusive fifth-order WENO scheme is shown in Fig. 16, right. The contours zoomed around the double Mach reflection region are given in Fig. 17. We can clearly see that the contact discontinuity resolution (manifested by the small scale structures) is significantly improved by the anti-diffusive modification to the fifth-order WENO scheme.

6. Concluding remarks

We have generalized the anti-diffusive flux corrections for sharpening contact discontinuities in [3] to high order finite difference WENO schemes. One- and two-dimensional scalar and system cases are all considered. The complication related to high order multi-stage Runge–Kutta time discretization is also addressed. Extensive numerical experiments, from one-dimensional scalar problems to two-dimensional systems, are performed to demonstrate the capability of the anti-diffusive WENO methods in maintaining high order accuracy and in sharpening contact discontinuities.

Acknowledgments

Research supported by ARO Grant W911NF-04-1-0291, NSF Grant DMS-0207451 and AFOSR Grant F49620-02-1-0113.

References

[1] D. Balsara, C.-W. Shu, Monotonicity preserving weighted essentially non-oscillatory schemes with increasingly high order of accuracy, Journal of Computational Physics 160 (2000) 405–452.
[2] F. Bouchut, An antidiffusive entropy scheme for monotone scalar conservation law, Journal of Scientific Computing 21 (2004) 1–30.
[3] B. Després, F. Lagoutière, Contact discontinuity capturing schemes for linear advection, compressible gas dynamics, Journal of Scientific Computing 16 (2001) 479–524.
[4] B. Després, F. Lagoutière, Numerical resolution of a two component compressible fluid model with interfaces and mixing zones, preprint.
[5] J. Glimm, J. Grove, X. Li, W. Oh, D.C. Tan, The dynamics of bubble growth for Rayleigh–Taylor unstable interfaces, Physics of Fluids 31 (1988) 447–465.
[6] J.B. Goodman, R.J. LeVeque, On the accuracy of stable schemes for 2D scalar conservation laws, Mathematics of Computation 45 (1985) 15–21.
[7] A. Harten, The artificial compression method for computation of shocks and contact discontinuities: III, Mathematics of Computation 32 (1978) 363–389.
[8] A. Harten, ENO schemes with subcell resolution, Journal of Computational Physics 83 (1989) 148–184.
[9] A. Harten, B. Engquist, S. Osher, S. Chakravathy, Uniformly high order accurate essentially non-oscillatory schemes: III, Journal of Computational Physics 71 (1987) 231–303.
[10] C. Hu, C.-W. Shu, Weighted essentially non-oscillatory schemes on triangular meshes, Journal of Computational Physics 150 (1999) 97–127.
[11] G. Jiang, C.-W. Shu, Efficient implementation of weighted ENO schemes, Journal of Computational Physics 126 (1996) 202–228.
[12] P.D. Lax, Weak solutions of nonlinear hyperbolic equations and their numerical computation, Communications on Pure and Applied Mathematics 7 (1954) 159–193.
[13] X. Liu, S. Osher, T. Chan, Weighted essentially non-oscillatory schemes, Journal of Computational Physics 115 (1994) 200–212.
[14] J.J. Quirk, A contribution to the great Riemann solver debate, International Journal for Numerical Methods in Fluids 18 (1994) 555–574.

[15] P.L. Roe, Some contribution to the modelling of discontinuous flows, Lectures in Applied Mathematics 22 (1985) 163–193.
[16] J. Shi, C. Hu, C.-W. Shu, A technique of treating negative weights in WENO schemes, Journal of Computational Physics 175 (2002) 108–127.
[17] J. Shi, Y.-T. Zhang, C.-W. Shu, Resolution of high order WENO schemes for complicated flow structures, Journal of Computational Physics 186 (2003) 690–696.
[18] C.-W. Shu, Essentially non-oscillatory and weighted essentially non-oscillatory schemes for hyperbolic conservation laws, in: B. Cockburn, C. Johnson, C.-W. Shu, E. Tadmor (Eds.), Advanced Numerical Approximation of Nonlinear Hyperbolic Equations, in: A. Quarteroni (Ed.), Lecture Notes in Mathematics, vol. 1697, Springer, Berlin, 1998, pp. 325–432.
[19] C.-W. Shu, High order finite difference and finite volume WENO schemes and discontinuous Galerkin methods for CFD, International Journal of Computational Fluid Dynamics 17 (2003) 107–118.
[20] C.-W. Shu, S. Osher, Efficient implementation of essentially non-oscillatory shock-capturing schemes, Journal of Computational Physics 77 (1988) 439–471.
[21] C.-W. Shu, S. Osher, Efficient implementation of essentially non-oscillatory shock capturing schemes II, Journal of Computational Physics 83 (1989) 32–78.
[22] K. Siddiqi, B. Kimia, C.-W. Shu, Geometric shock-capturing ENO schemes for subpixel interpolation computation and curve evolution, Graphical Models and Image Processing (CVGIP:GMIP) 59 (1997) 278–301.
[23] G. Sod, A survey of several finite difference methods for systems of nonlinear hyperbolic conservation laws, Journal of Computational Physics 43 (1978) 1–31.
[24] P.K. Sweby, High resolution schemes using flux limiters for hyperbolic conservation laws, SIAM Journal on Numerical Analysis 21 (1984) 995–1011.
[25] V.A. Titarev, E.F. Toro, ENO and WENO schemes based on upwind and centered TVD fluxes, Computers and Fluids, to appear.
[26] E.F. Toro, V.A. Titarev, TVD fluxes for the high order ADER schemes, Journal of Scientific Computing, to appear.
[27] P. Woodward, P. Colella, The numerical simulation of two-dimensional fluid flow with strong shocks, Journal of Computational Physics 54 (1984) 115–173.
[28] H. Yang, An artificial compression method for ENO schemes: the slope modification method, Journal of Computational Physics 89 (1990) 125–160.
[29] Y.-N. Young, H. Tufo, A. Dubey, R. Rosner, On the miscible Rayleigh–Taylor instability: two and three dimensions, Journal of Fluid Mechanics 447 (2001) 377–408.
[30] Y.-T. Zhang, J. Shi, C.-W. Shu, Y. Zhou, Numerical viscosity and resolution of high-order weighted essentially nonoscillatory schemes for compressible flows with high Reynolds numbers, Physical Review E 68 (2003) 046709.